

Chapter 3

Optical Interactions



Semiconductor processing of a Si wafer described in Chap. 2 creates optimum fields and surfaces to facilitate efficient conversion of absorbed light in Si wafer into external current. Figure 3.1 illustrates how reflection and transmission losses contribute to reduced performance purely from optical perspectives. In a monofacial solar cell, light from the back surface is reflected, and some of it eventually escapes from the wafer following multiple internal reflections especially in near-IR spectral region. A good solar cell combines minimum reflection losses with maximum absorption. These requirements are examined in terms of texture dimensions. Conversion of absorbed light into photocurrent is investigated using surface photovoltage effect. Alternate optical characterization schemes based on photoconductive decay and photoluminescence imaging will be presented.

3.1 Geometrical Optics

Crystalline silicon is characterized by its high refractive index and weak near-IR absorption resulting in high reflection (Fig. 3.2a) and transmission losses (Fig. 3.2b) [1]. Si reflectance is high ~52% in the UV region and decreases to ~33% through most of the visible to near-IR range. Spectral response reveals UV-visible light absorption close to the top surface. At longer wavelengths, particularly near the band edge, the absorption is much weaker, i.e., absorption depth of ~100 μm at 1- μm wavelength. In most solar cells, the n/p junction, formed within ~0.1–0.5 μm of the top surface, collects almost 100% of the photo-generated carriers in the UV-visible spectral range. In near-IR spectral range, a fraction of carriers is lost to bulk recombination due to material defects. Well-designed solar cells with appropriate anti-reflection films [2] convert almost 100% of the UV-visible radiation into current; however, anti-reflection films don't improve near-IR absorption. A highly effective approach aimed at enhancing near-IR absorption is based on light trapping using geometrical optics through random pyramidal texturing of (100) Si surfaces

Fig. 3.1 Light incidence, reflection, absorption, and transmission through a Si wafer

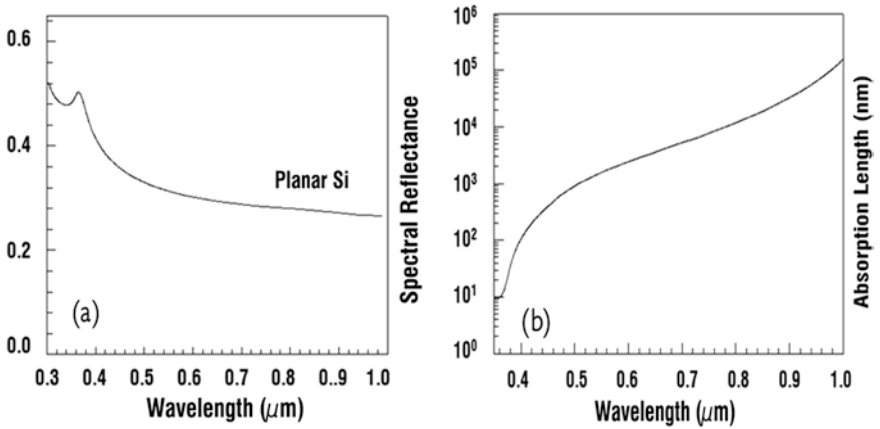
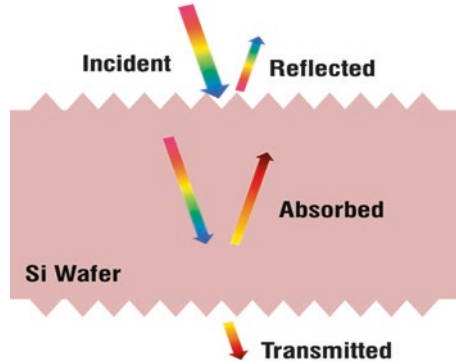


Fig. 3.2 Spectral reflectance (a) and absorption depth in Si (b) plotted as a function of wavelength

[3]. In these structures, enhanced absorption is achieved by oblique coupling of light into the semiconductor. Typical feature dimensions \gg larger than optical wavelengths take advantage of the fact that due to large refractive index n of Si, light traveling at angles $>\theta_c = \sin^{-1}(1/n)$ is subjected to total internal reflection. These methods have been extensively investigated and contribute to optical path length enhancement of ~ 1.3 relative to a planar surface [4].

An alternative approach aimed at enhanced absorption has also been investigated and is better understood with a review of statistical mechanics [5]. In a weakly absorptive medium, the number density of photons absorbed at a given frequency ω is proportional to the product of four factors:

$$\text{Absorbed photon density} \cong u(\omega) * \alpha * \frac{c}{n} * \frac{d^3k}{d\omega}, \tag{3.1}$$

where

$$u(\omega) = \frac{1}{\exp\left(\frac{h\omega}{k_B T}\right) - 1}, \quad (3.2)$$

is the Bose occupation number for solar radiation, α is the absorption coefficient of the material, c is the velocity of light in vacuum, n is material refractive index, and k is the wave vector of light. $\frac{1}{n} * \frac{d^3 k}{d\omega}$ is the effective density of states $\rho(\omega)$ for absorption. In an isotropic medium, a photon state is represented by a plane wave of definite polarization and propagation vector. The number density of these states is proportional to $4\pi k^2$, where $k = 2\pi/\lambda$. In an isotropic medium of refractive index n , $k = n * k$ so that the density of states in a medium is larger by a factor of n^2 . These extra photon states are visualized as light rays traveling in an optically dense medium at angles $>\theta_c$. In a detailed statistical analysis, Yablonovitch predicted absorption enhancement in textured surface by as much as a factor of $4n^2$ over a planar surface [6]. However, in order to reach this statistical mechanics limit, surface texture must fully randomize incident light to fill internal optical phase space. Deckman et al. [7] have demonstrated that optimum random textures have dimensions slightly larger than the wavelength of light in the material. If the lateral dimensions of the microstructure are too large, light is specularly reflected reducing internal randomization. If the lateral dimensions are much smaller than the wavelength of light, light scattering is also not effective because of the inability to resolve microstructure, which again reduces internal randomization. Therefore, in order to achieve maximum possible absorption enhancement, a precise balance between randomness and microstructure dimension must be realized.

3.2 Diffractive Optics

Optical scattering of light incident on a periodic surface is described in terms of diffraction grating equation given by [8]

$$\sin\theta_m = \sin\theta_i + m \frac{\lambda}{d}, \quad (3.3)$$

where d is the spatial period of material, λ wavelength of incident light, θ_i incident angle, and θ_m angle of diffracted beam; $m = 0, \pm 1, \pm 2, \dots, \pm m$. Assuming normal incidence for a material of refractive index, n , the diffraction angle, θ_m , is given by

$$\theta_m = \sin^{-1} \left[m \frac{\lambda}{(n * d)} \right]. \quad (3.4)$$

Equation 3.4 can be used to illustrate angular distribution of transmitted diffraction orders inside a material of refractive index, n , as a function of the ratio $\frac{\lambda}{(n * d)}$

as illustrated in Fig. 3.3. The first case is similar to geometrical optics with surface features much larger than the wavelength (Fig. 3.3a). For such surfaces, diffraction angles are small and transmitted diffraction orders propagate approximately normal to the surface. The second case considers surface features comparable to optical wavelengths and leads to large angle scattering of diffracted orders inside Si. This configuration is referred to diffractive scattering and can potentially fill the k-space described above [9]. The third configuration refers to surface features significantly smaller than optical wavelengths; for such surfaces, there are no diffraction orders. This configuration is leading to physical optics and waveguides [10]; it will be discussed in later sections.

In thin Si wafers, oblique coupling of light is desirable in order to enhance its path length to generate photocurrent closer to the surface. Figure 3.4 illustrates optical path length enhancement for a diffraction order propagating at an angle, θ_m , in a wafer of thickness, t , with respect to the normal; the optical path length is given by

$$\text{Optical path length} = \frac{t}{\cos \theta_m}. \quad (3.5)$$

Therefore, for large angles, OPL enhancement is much larger than can be achieved in geometrical optics, i.e., for $\theta_m = 75^\circ$, OPL is increased by ~ 4 times the wafer thickness. For c-Si, refractive index at $\lambda=1 \mu\text{m}$ is 3.7 [11], the number of diffraction orders at $0.68\text{-}\mu\text{m}$ period will be $4 (\pm 1, \pm 2)$, and at $0.29\text{-}\mu\text{m}$ period, the number of diffraction orders will be $2 (\pm 1)$; some of these will propagate at angles approaching 90° (Fig. 3.5).

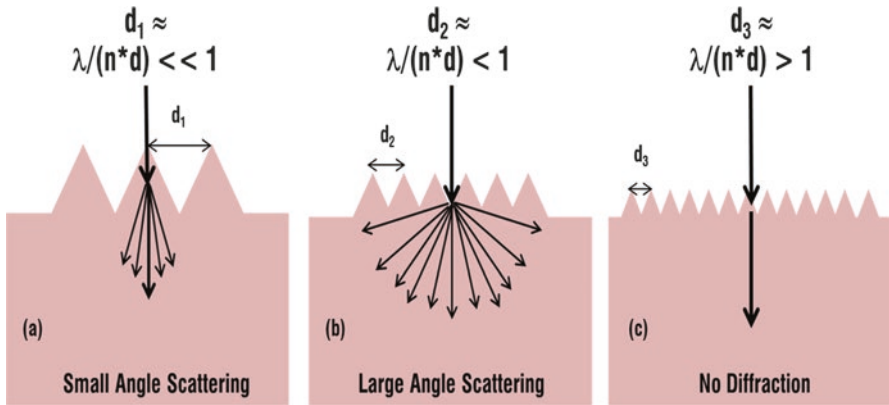


Fig. 3.3 Transmitted diffraction orders incident a material of refractive index n illustrated for (a) $\lambda \ll d$, (b) for $\lambda \sim d$, and (c) $\lambda \gg d$

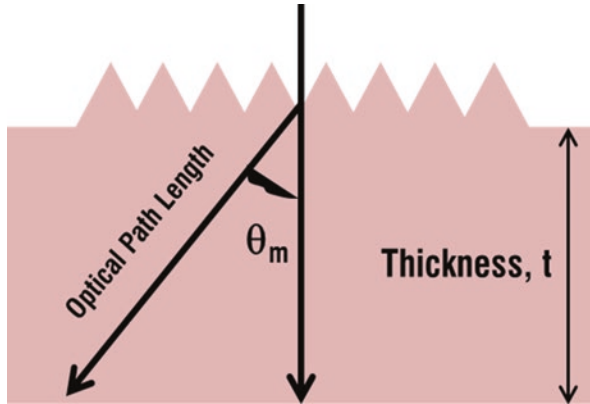


Fig. 3.4 Optical path length variations with angle inside a weakly absorptive material of thickness t

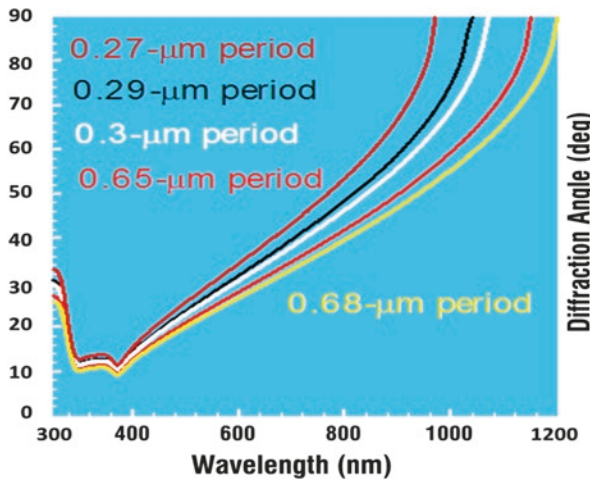


Fig. 3.5 Transmitted diffraction order angles plotted as a function of wavelength inside Si substrates for periods in 0.27–0.68- μm range

3.3 Optical Response of Subwavelength Periodic Structures

Light interaction with subwavelength periodic structures has been extensively investigated. Wilson and Hutley investigated 2D moth eye patterns in photoresist and metals [12]. They observed broadband anti-reflection behavior from both surfaces. The optical response was observed to be a function of pattern dimensions and polarization of incident light. Enger and Case demonstrated broadband antireflective characteristics of 300-nm period quartz grating with significant enhancement in transmission [13]. Profile of the periodic structure dominated optical response; maximum transmission was observed for triangular profiles. Zaidi et al. [14]

demonstrated broadband anti-reflection characteristics of Ag-coated 1D sub- μm period structures. The reflection was demonstrated to be a function of grating depth, profile, and incident light polarization. K. Knop observed that deep, rectangular-profiled quartz gratings behaved as color filters in zero-order transmission, and the response was similar for both polarizations for grating periods $\sim 1.4\text{--}2.0\ \mu\text{m}$ [15]. Ping Sheng et al. carried out exact numerical calculations for a thin-film, wavelength-selective solar cell [5]. The model calculations showed 2-mA/cm^2 enhancement over the planar surface for 1D grating and $3.5\text{--}4\ \text{mA/cm}^2$ for a 2D grating. By using randomly textured surfaces, Deckman et al. reported on short-circuit density ($\sim 3\ \text{mA/cm}^2$) increase in thin-film solar cells [7]. Heine and Morf have recently reported sub- μm grating application to improve solar cell performance. This approach relies on blazing properties of grating structures to improve absorption in IR region [16]. Later on, Zaidi et al. reported on broadband absorptive properties of Si nanostructures for application in Si solar cells [17].

Modeling of periodic structures is involved and computer intensive. Figure 3.6 identifies three regions in terms of optical interaction with the material. Rayleigh developed one of the earliest models; his approach was applicable only to shallow gratings and did not consider fields within the structure [18]. This was addressed by Botten et al., by deriving an exact eigenfunction for the electric field inside the grating region; the eigenvalues for this function are used during the electric field expansion of the grating region by matching boundary conditions at three interfaces; strength of the modellies in prediction of guided and anti-guided modes responsible for optical enhancement [19].

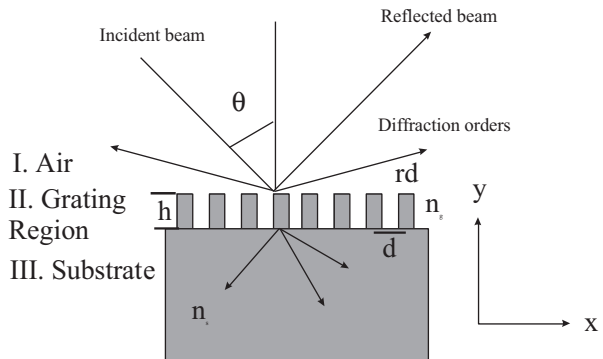
The electric field in region I is defined by

$$E^I(x,y) = e^{i(\alpha x - \beta y)} + \sum_k R_k e^{i(\gamma_k - r_k y)}, \tag{3.6}$$

where R_k 's are diffraction orders and R_0 is the zero-order reflected beam. Electric field in region III is

$$E^{III}(x,y) = \sum_m T_m e^{i(\gamma_m - t_m y)}, \tag{3.7}$$

Fig. 3.6 Optical configuration designed to determine optical response of a periodic structure



T_m 's are transmitted diffraction orders with T_0 being the zero-order transmitted beam. Electric field in region II is given by

$$E^{\text{II}}(x,y) = \sum_l \frac{1}{c_l} X_l(x) [A_l e^{igly} + B_l e^{-igly}], \quad (3.8)$$

where $X_l(x)$ are eigenfunctions of the grating region. These equations are numerically solved to determine energy distribution within the reflected, transmitted, and grating regions. This model provides physical insights; however, it is not commercially available and is not easily applicable to arbitrary profiles.

Moharam and Gaylord developed an alternate numerical model based on rigorous coupled-wave analysis (RCWA) in which the electric field inside the grating region is represented in terms of Fourier series [20]. The numerical approach consisted of slicing grating profile into many layers parallel to the surface to provide accurate results, but perhaps with little physical insight. Alternatively, an effective medium theory has also been developed that assumes continuous refractive index variation from the top of the grating surface to the substrate in much the same manner as the index variation in a graded index thin-film structure [2, 21]. This theory is particularly suitable to triangular or sinusoidal profiles. Grating software, GSOLVERTM, based on the RCWA model is commercially available and will be used in later sections for diffractive and physical optics analysis of optical response of subwavelength structures [22].

3.4 Polarization and Anti-reflection Response of Subwavelength Periodic Structures

High aspect ratio, nanoscale linewidth subwavelength grating structures are capable of tailoring reflectance profile to any desired spectral range [23–29]. Optical response of a wide range of one-dimensional (1D) and two-dimensional (2D) structures etched in c-Si substrates is evaluated over a wide range of grating parameters. Normal incidence measurements of grating structures were carried out with respect to incident light parallel (TE) and perpendicular (TM) to grating lines. All data was normalized with respect to planar Si reflection under identical conditions

Figure 3.7a plots normal incidence zero-order reflectance response from 300-nm period, 50-nm linewidth grating etched to a depth of 1000 nm (Fig. 3.7b). A broadband reflection reduction is observed for both polarizations. For TM polarization, broadband reflection reduction is observed in 400–600-nm spectral range followed by rapid increase in 600–800-nm range. For the TE-polarized light, reflection exhibits a broadband reduction; overall reflection is lower than that for the TM-polarized light. Figure 3.8a plots normal incidence zero-order reflectance measurements from 500-nm period, 130-nm linewidth grating etched to a depth of 1000 nm (Fig. 3.8b). A broadband reflection reduction is observed for both polarizations. For TM polarization, reflection is reduced below 400 nm; at longer wavelengths, reflection

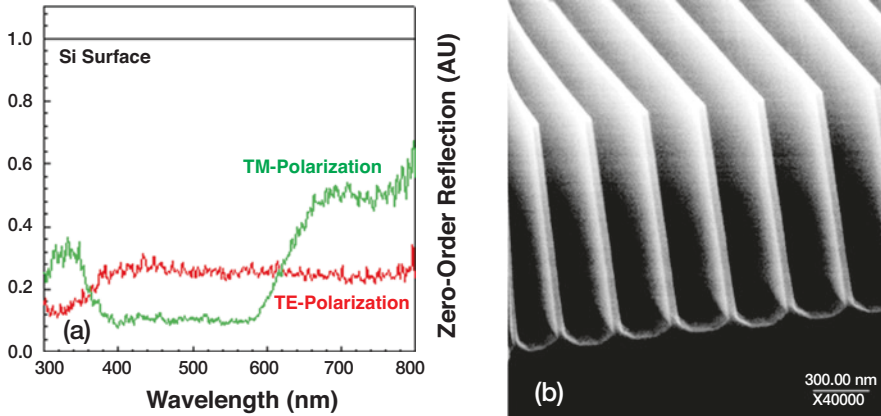


Fig. 3.7 Polarization-dependent reflectance plotted as a function of wavelength (a) for 300-nm period, 50-nm linewidth 1D grating (b)

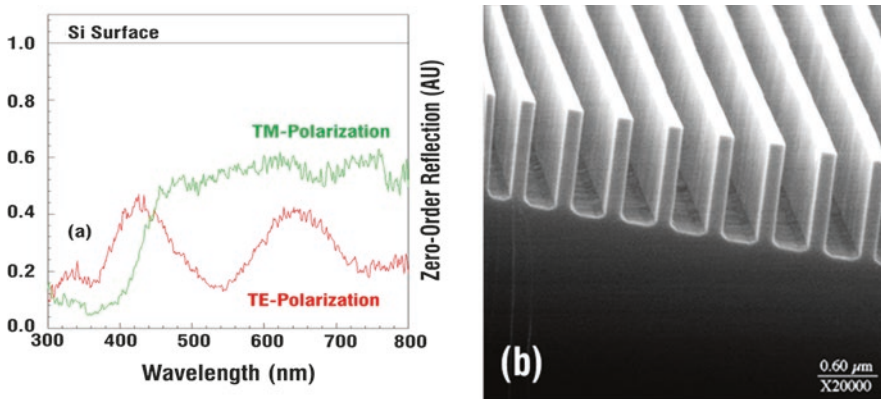


Fig. 3.8 Polarization-dependent reflectance plotted as a function of wavelength (a) for 500-nm period, 130-nm linewidth 1D grating (b)

remains constant. For the TE-polarized light, reflection exhibits a resonant structure with reflection minima at ~ 350 nm, 550 nm, and 750 nm wavelengths; overall reflection is lower than the TM-polarized light. Figure 3.9a plots normal incidence zero-order reflectance measurements from 1000-nm period, 330-nm linewidth grating etched to a depth of 1000 nm (Fig. 3.9b). A broadband reflection reduction is observed for both polarizations. For TM polarization, reflection minima are observed at ~ 300 nm, 450 nm, and 550 nm wavelengths. For the TE-polarized light, reflection exhibits similar structure with reflection minima at ~ 350 nm, 450 nm, 580 nm, and 750 nm wavelengths; overall reflection response is similar at both polarizations. Reflection response comparison of these three structures reveals a transition from broadband to resonant behavior. This may be attributed to a combination of

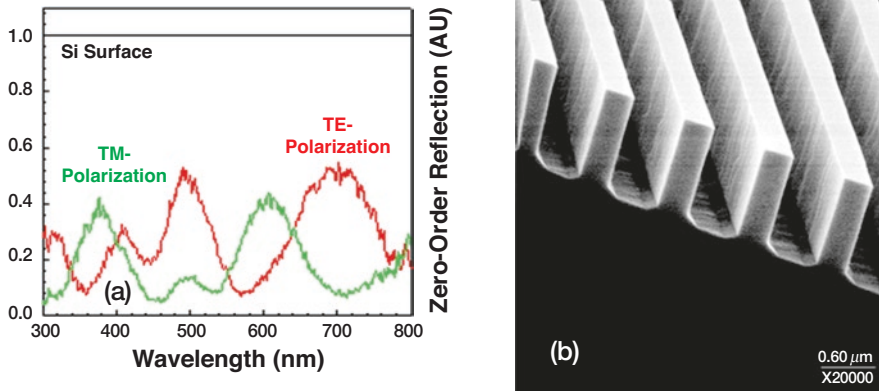


Fig. 3.9 Polarization-dependent reflectance plotted as a function of wavelength (a) for 1000-nm period, 330-nm linewidth 1D grating (b)

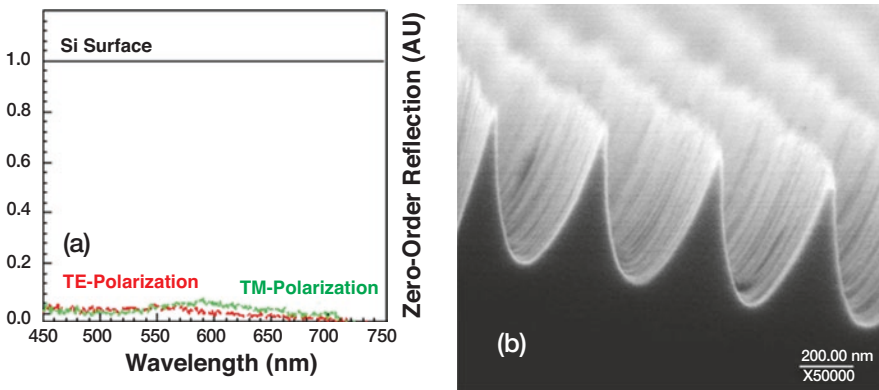


Fig. 3.10 Polarization-dependent reflectance plotted as a function of wavelength (a) for 440-nm period, 20–120-nm linewidth triangular profile 1D grating (b)

diffractive and physical (waveguide) optics interactions. At 1000-nm period, there are multiple radiative diffraction orders in 400–800-nm spectral range in Si; therefore, some of the reflection minima may be attributed to coupling of incident light into higher diffraction orders. In contrast, for the 300-nm period, no propagating diffraction orders are available in air, only transmitted orders are propagating inside Si.

Polarization-dependent reflection response of one-dimensional (1D) and two-dimensional (2D) triangular gratings has also been evaluated. Figure 3.10a plots normal incidence zero-order reflectance measurements from 440-nm period triangular-profiled structure etched to a depth of ~600 nm with linewidth varying from ~20 nm at the top to ~120 nm at the bottom (Fig. 3.10b). Substantially reduced broadband reflection reduction, independent of polarization, is observed. Figure 3.11a plots normal incidence zero-order reflectance measurements from

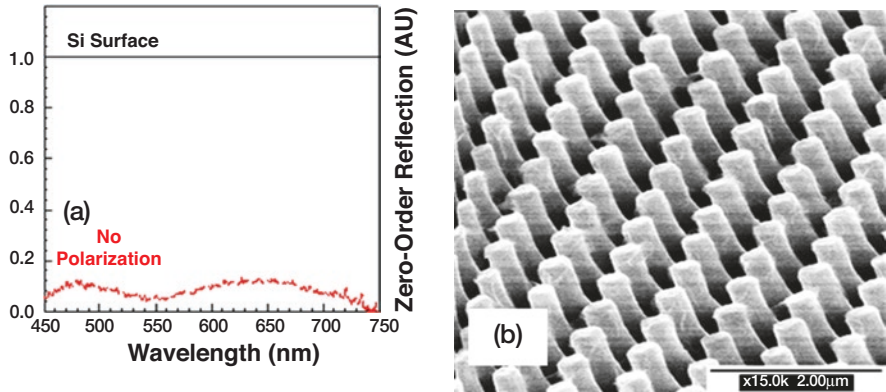


Fig. 3.11 Polarization-independent reflectance plotted as a function of wavelength (a) for 700-nm period, 300-nm linewidth cylindrical profile 2D grating (b)

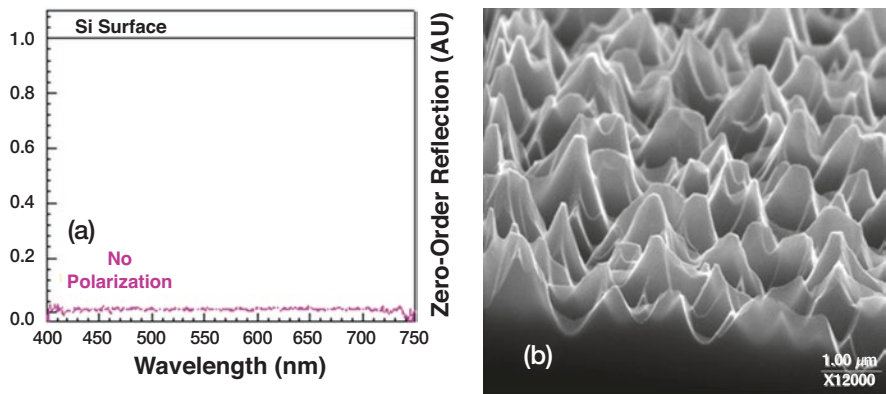


Fig. 3.12 Polarization-independent reflectance plotted as a function of wavelength (a) for 2D randomly textured surface with depths and linewidths in $\sim 500\text{--}2000$ nm range (b)

~ 700 -nm period, 2D grating etched to a depth ~ 1000 nm with a cylindrical profile (Fig. 3.11b). Due to the two-dimensional nature of the structure, unpolarized light was used for reflection measurements. Reflection was substantially lower than the planar surface with broad reflection minima at ~ 450 nm, 550 nm, and 700 nm. Finally, Fig. 3.12a plots reflection response of randomly etched 2D pattern with periods and depths in $\sim 500\text{--}1000$ -nm range and linewidth in $\sim 50\text{--}350$ nm range; profiles were approximately triangular (Fig. 3.12b). This structure exhibits the lowest reflectance and will be discussed in more detail in the section on randomly textured surfaces.

3.4.1 Hemispherical Reflectance

Normal incidence, polarization-dependent zero-order spectral reflection measurements do not provide enough information regarding energy distribution among reflected and transmitted diffraction orders. Absolute hemispherical measurements collect all the scattered radiation from the sample. Hemispherical reflectance of structures displayed in Figs. 3.7, 3.8, 3.9, 3.10, 3.12 and 3.13 were also carried out. Figure 3.14 plots hemispherical reflection measurements of the 1D grating structures; for reference, planar Si surface reflection is also included. Salient features of these measurements are summarized below.

- (i) Reflection from 1- μm grating is almost comparable to that of planar Si.
- (ii) Increase in reflectance in 1000–1200-nm region is due to transmitted light coupled out of the Si and grating samples.
- (iii) Reflection is lowest in the UV-VIS region for the 300-nm period sample.
- (iv) All samples exhibit narrowband reflectance bands.
- (v) Reflectance is reduced as periods and linewidths decrease.

For the 300-nm period (blue line), the reflection dip at $\lambda \sim 320$ nm probably corresponds to $\theta_{\pm 1} \sim 90^\circ$ in air. The reflectance minimum at $\lambda \sim 1000$ nm probably corresponds to $\theta_{\pm 1} \sim 90^\circ$ in Si. For 500-nm period (green line), pronounced reflectance dip at $\lambda \sim 500$ nm probably corresponds to $\theta_{\pm 1} \sim 90^\circ$, and the second dip at ~ 900 nm appears to correspond to $\theta_{\pm 2} \sim 90^\circ$ inside Si. The reflection minimum for 1.0- μm (red line) period grating at $\lambda \sim 0.92$ μm is observed which approximately corresponds to $\theta_{\pm 1} \sim 90^\circ$ in air. At this period, there are a large number of diffraction orders inside Si. Some of the dips in the reflectance in 400–800-nm spectral range

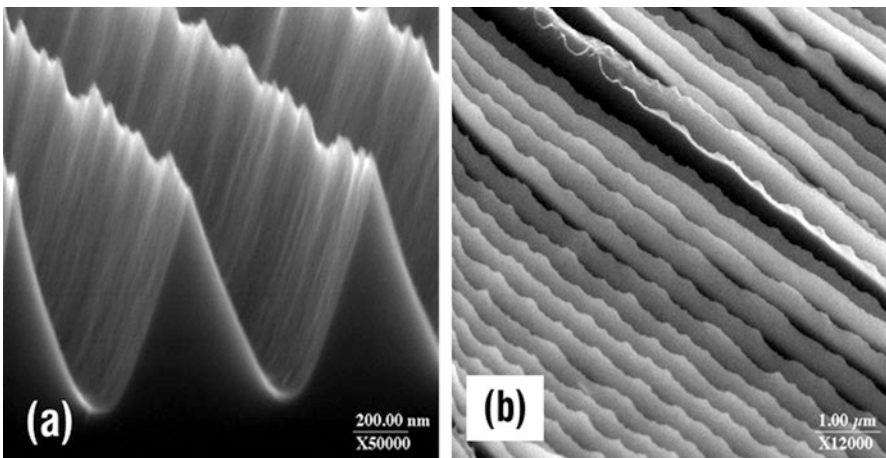


Fig. 3.13 Scanning electron microscope pictures of 640-nm period 1D grating with linewidth in ~ 20 –120 nm range etched to a depth of 600 nm: cross-sectional profile (a) and top view (b)

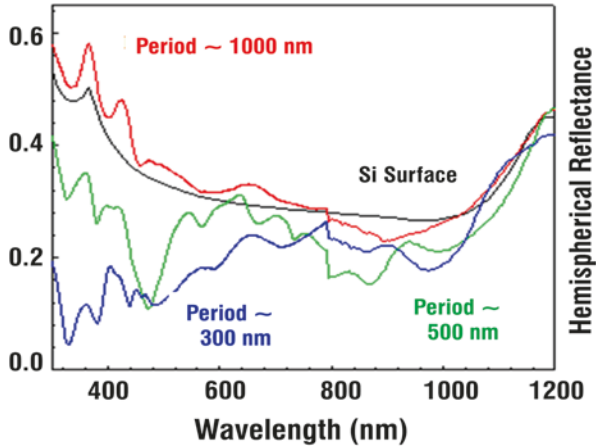


Fig. 3.14 Hemispherical spectral reflectance measurements from 1D gratings and planar Si surface plotted as a function of wavelength

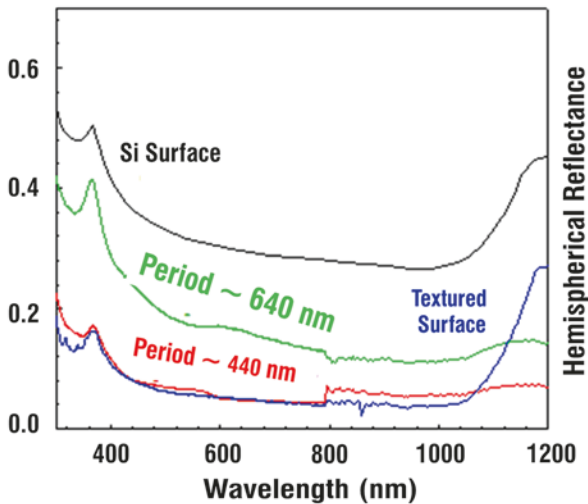


Fig. 3.15 Hemispherical spectral reflectance of triangular profile 1D gratings and randomly textured surface plotted as a function of wavelength; planar Si response is also plotted for reference

probably correspond to higher-order non-radiative diffraction orders as well as waveguide coupling within grating structures.

Figure 3.15 plots hemispherical spectral reflectance measurements of two 1D grating structures; for comparison, reflection from bare and randomly textured Si surface is also shown. It is seen that these surfaces exhibit broadband anti-reflection behavior, and overall reflectance decreases as grating period and linewidths are reduced from 0.64 μm to 0.44 μm . Figures 3.10b and 3.13 display SEM profiles of

the 1D gratings used for measurements in Fig. 3.15. The 640-nm period grating has a depth of ~ 600 nm with linewidth variation from ~ 60 nm at the top to ~ 300 nm at half grating depth. The 440-nm period grating has a depth of ~ 600 nm with linewidth variation from ~ 15 nm at the top to ~ 100 nm at half grating depth. Thus, it appears that reflection is reduced more effectively by linewidths in ~ 20 – 100 nm linewidth range. An interesting feature is complete absorption even at 1000–1200-nm spectral range for 1D gratings in comparison with the randomly textured surface.

In order to better understand optical interactions, 1D gratings at 300–1000-nm periods etched in 1.6- μm -thick c-Si film on sapphire substrate. In this case, absorption in the thin film was calculated by using the formula

$$A = 1 - R - T, \quad (3.9)$$

where total reflection, R , and transmission, T , were measured experimentally. Figure 3.16 plots absorption measurements from all three structures; absorption in planar film is also included for comparison. Salient features of these measurements are summarized below.

- (i) Observation of Fabry-Perot resonances due to interference between front and rear-reflected light beams
- (ii) Lowest absorption in planar film
- (iii) Higher absorption in 300–600-nm spectral region independent of period
- (iv) Highest absorption at 300-nm period
- (v) Resonant structure for 500- and 1000-nm periods

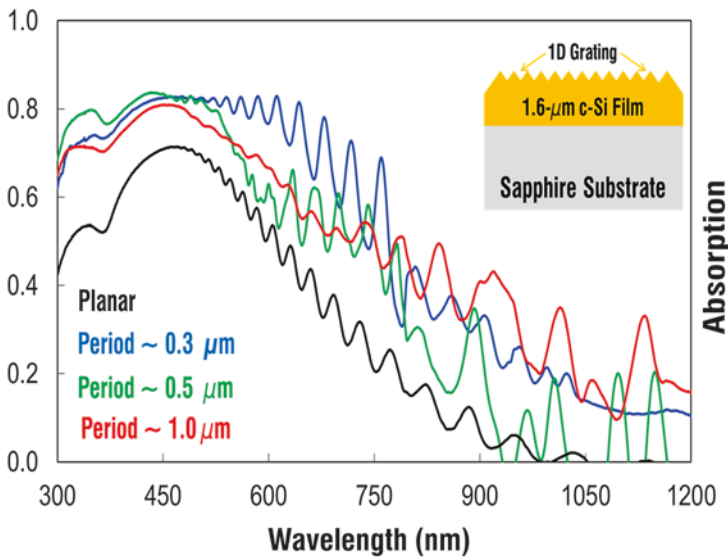


Fig. 3.16 Hemispherical absorption plotted as a function of wavelength in thin-film and 1D grating configurations; inset identifies the thin-film configuration

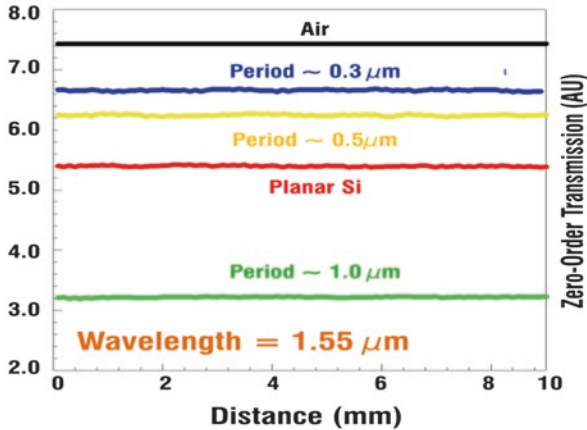


Fig. 3.17 Normal incidence transmission at 1.55- μm wavelength plotted as a function of translation for three 1D grating structures; for reference transmission in air and through planar Si has also been included

Highest absorption in 300-nm period is attributed to the absence of diffractive losses. Comparable absorption in 300–500-nm region is likely due to waveguide mechanisms. Higher absorption relative to planar film is a combination of oblique diffractive coupling and physical waveguide mechanisms (physical optics). In order to assess the diffractive and anti-reflection effects, normal incidence transmission measurements were carried out at 1.55- μm wavelength. Figure 3.17 plots transmitted signal as a function of translation across 10-mm width of the sample; transmission signal in air and planar Si has also been plotted for reference. Assuming 100% transmission in air, it is possible to summarize transmission variations due to light interactions at air/Si interface.

- (i) Transmission through planar Si is $\sim 73\%$ due to 27% reflection loss.
- (ii) Transmission through 1000-nm period 1D grating is $\sim 57\%$ due to 43% reflection loss.
- (iii) Transmission through 500-nm period 1D gratings is $\sim 84\%$ due to 16% reflection loss.
- (iv) Transmission through 300-nm period 1D gratings is $\sim 89\%$ due to 11% reflection loss.

Figure 3.18 illustrates light interaction in terms of energy distribution into diffraction orders. At $\lambda = 1.55\text{-}\mu\text{m}$, ratio λ/d is >1 for grating periods in 0.3–1.0- μm range; therefore, there are no energy losses to diffraction orders in air. The situation inside Si is different due to its high refractive index. At 1- μm period, there are first and second diffraction orders propagating at $\pm 25^\circ$ and $\pm 57^\circ$, respectively. At 0.5- μm period, there are two diffraction orders propagating at $\pm 57^\circ$; for 0.3- μm period, there are no diffraction orders. Therefore, highest transmission is observed for smallest grating, albeit without any internal scattering and grating behaving as AR

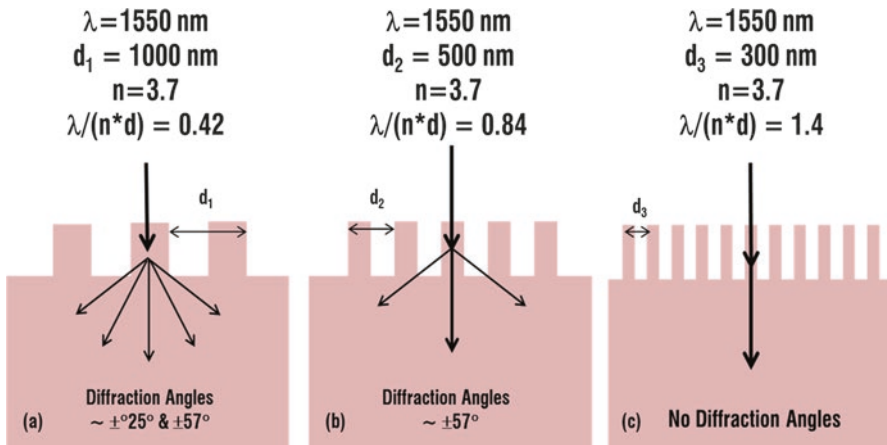


Fig. 3.18 Normal incidence transmission at 1.55- μm wavelength illustrated in terms of transmitted diffraction orders for (a) 1000-nm, (b) 500-nm, and (c) 300-nm period gratings

film. For the 0.5- μm period, transmission is only slightly lower due to the fact that energy coupling at ± 1 diffraction orders propagating at 57° is negligible. However, for the 1- μm period, ± 1 diffraction orders propagating at 25° carry substantial energy, thus accounting for substantial reduction in zero-order transmission. For solar cells, large internal scattering is desirable in order to enhance absorption through oblique scattering; therefore, grating periods should be comparable to light wavelength.

3.5 Software Simulations Using GSOLVER™

Commercially available GSOLVER™ software has been used to validate light interactions with subwavelength structures. Grating response was evaluated in terms of diffractive and physical optics.

3.5.1 Diffractive Optics for Enhanced IR Absorption

A highly effective way of enhancing near-IR absorption in Si is based on oblique coupling through diffraction. With suitable grating profile, transmitted light inside Si is directed at oblique angles, while the coupling of light into the zero order is significantly reduced. With the help of GSOLVER™ software, a wide range of 700-nm period 1D grating structures was investigated including blazed and rectangular profiles illustrated in Fig. 3.19. Simulations revealed that almost $\sim 100\%$ of the energy can be transferred into transmitted diffraction orders inside Si as long as

Fig. 3.19 One-dimensional blazed (a) and rectangular (b) profiles used for estimating diffraction efficiency as a function of depth

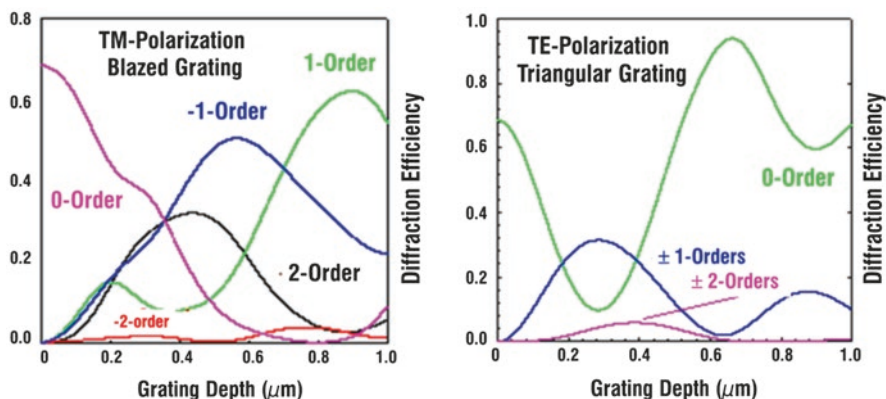
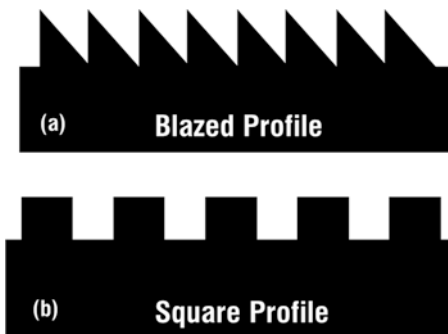


Fig. 3.20 Diffraction efficiency, for 0.65-μm period blazed (left) and rectangular (right) 1D gratings, plotted as a function of depth

propagation angle is $\leq 60^\circ$ with respect to the surface normal. At higher propagation angles, most of the energy was coupled back into the zero order. Figure 3.20 plots energy distribution as a function of depth for blazed as well as triangular 1D grating structures. Coupling efficiency into diffraction orders is a function of grating depth with almost ~100% of the incident energy transfer into a transmitted orders at certain depths. This behavior is strongly dependent on incident polarization and grating duty cycle.

In order to verify accuracy of simulations, Si gratings at 700-nm period were etched with rectangular profiles and increasing depths. Figure 3.21a shows SEM profile of rectangular profile grating etched to a depth of ~0.24 μm and linewidth ~0.32 μm. Figure 3.21b displays SEM profile of the same grating structure etched to a depth of ~0.45 μm and linewidth ~0.35 μm. Figure 3.21c shows SEM profile of the same grating etched to a depth of ~0.72 μm and linewidth ~0.37 μm. Figure 3.22a plots normalized reflection measurements for TM-polarized light. Overall reflection reduction as a function of etch depth is observed. For the 0.24-μm depth sample, a slight cusp is seen at ~700-nm wavelength at which the first

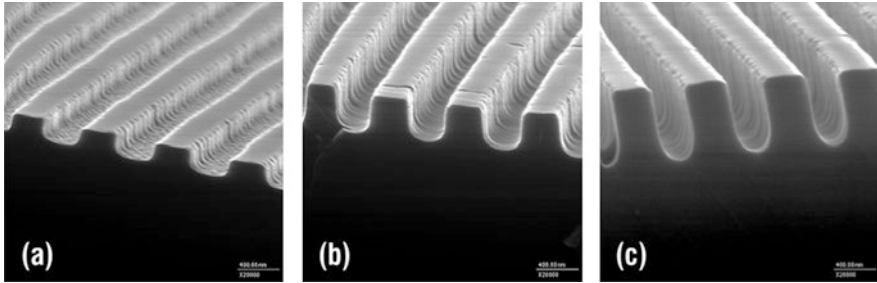


Fig. 3.21 SEM pictures of 700-nm period gratings etched in Si to depths of $\sim 0.2 \mu\text{m}$ (a), $\sim 0.4 \mu\text{m}$ (b), and $\sim 0.73 \mu\text{m}$ (c)

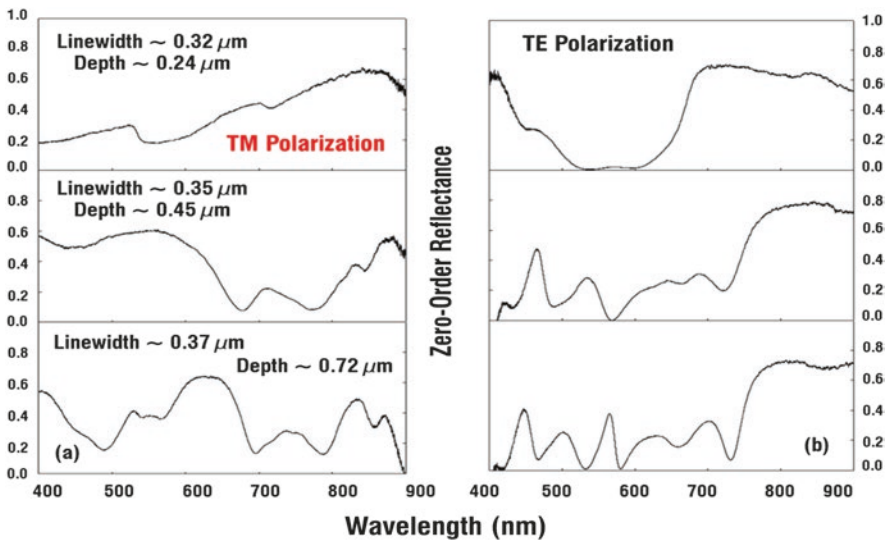


Fig. 3.22 Zero-order TM (a) and TE (b) reflectance measurements of 700-nm period gratings plotted as a function of wavelength for varying duty cycles and depths

diffraction order in air becomes evanescent. For the 0.45-μm depth, a broad resonance is seen in 650–850-nm region. For the 0.72-μm depth sample, broad reflection minima are observed at $\sim 480 \text{ nm}$, 680 nm , 780 nm , and $\sim 880 \text{ nm}$. Figure 3.22b plots normalized reflection measurements for TE-polarized light. For the 0.24-μm depth sample, a broad minimum in reflection is observed seen between 450 nm and 700 nm wavelengths. For the 0.45-μm depth sample, reflection is almost zero at $\sim 580 \text{ nm}$; in general reflection varies substantially with wavelength. For the 0.72-μm depth sample, a number of reflection minima are observed in 400–800-nm spectral range.

Grating reflection response was modeled based on profiles displayed in Fig. 3.21. Figure 3.23 plots both TE and TM reflection measurements for a

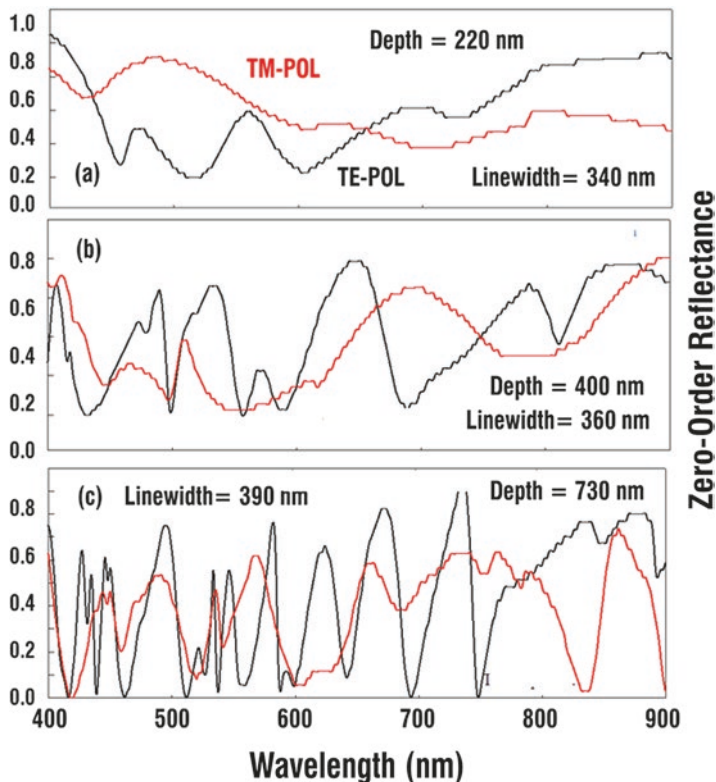


Fig. 3.23 Zero-order TM and TE calculated reflectance plotted as a function of wavelength for 220-nm (a), 400-nm (b), and 730 nm (c) gratings

220-nm deep grating at a linewidth of ~ 340 nm. Comparison with experimental data reveals good agreement with TE-polarized reflectance; however, agreement with TM reflectance is poor. For the 400-nm deep grating, experimental and calculated reflectance matches poorly. For the 720-nm depth grating, agreement between experimental and calculated reflectance results is poor. Reflectance response is highly sensitive to linewidth and depth variations. Since these gratings have structural variations, it is likely that measured reflection is a composite of multiple linewidths and depths. In general, trend towards waveguide type resonances at deeper gratings matches well with experimental data.

3.5.2 Physical Optics for Enhanced IR Absorption

In shallow ($< \lambda/4$) gratings, most of the energy is coupled out into diffraction orders. As grating depth increases, grating structure accommodates larger number of waveguide modes. For deep ($> \lambda$) grating structures, each of the grating line may be

considered as a symmetric waveguide supporting an increasing number of modes determined by its linewidth and depth. Within grating structures, the optical absorption is, A_g , given by

$$\text{Absorption, } A_g = 1 - \sum_i R_i - \sum_j T_j, \quad (3.10)$$

where the summation indices i and j include all the radiative and evanescent diffraction orders in air and Si. Figure 3.24 plots TE-polarized grating absorption as function of depth for the 0.7- μm period grating with 50% duty cycle at $\lambda = 1.0 \mu\text{m}$. The absorption variation with depth has been fitted using a quadratic polynomial given by

$$A = A_0 + A_1 * h + A_2 * h^2, \quad (3.11)$$

where h is grating depth, $A_0 = -0.0057$, $A_1 = 0.0255$, and $A_2 = -0.0005$. The absorption is a complicated function of depth and appears to increase very slowly for grating depths $<15 \mu\text{m}$, but for longer depths, the absorption increases linearly with h .

3.5.3 Physical Optics for Enhanced IR Absorption in Thin Films

As Si PV technology transitions from wafer to thin films, incomplete optical absorption will limit solar cell performance. Application of physical optical approach based on subwavelength 1D and 2D structures integrated with Si film thicknesses in

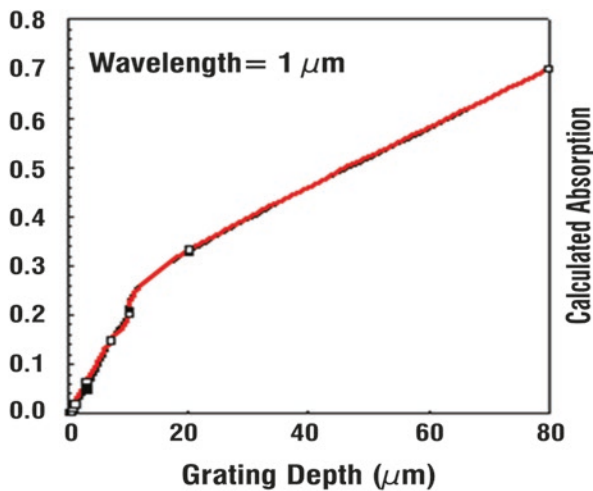


Fig. 3.24 Absorption in 0.7- μm period Si grating structure as a function of depth at $\lambda = 1.0 \mu\text{m}$; the red line represents a second-order polynomial fit to the calculated data

$\sim 30\text{--}50\ \mu\text{m}$ range was investigated. Figure 3.25 describes three thin-film configurations employed for optical absorption calculations. One-dimensional gratings exhibited significant absorption, although the response was polarization dependent. Since the sunlight is unpolarized, 2D grating structures were used for simulations. For all simulations, total thickness was kept fixed at $30\ \mu\text{m}$. For structures with an underlying Si film on an Al substrate, the optical absorption is calculated for grating depth plus thickness varying from 0 to $25\ \mu\text{m}$ with the underlying film thickness fixed at $5\ \mu\text{m}$. In subwavelength 2D grating calculations, it is critical that the calculation convergence is established. Solution convergence was investigated as a function of series summation indices up to ~ 20 . Figure 3.26 plots convergence data for the two optical configurations described in Fig. 3.25. Absorption results in Fig. 3.26 reveal that for 2D grating structure without underlying Si film (Fig. 3.25a), convergence at $\lambda \sim 1.0\ \mu\text{m}$ is not achieved until at least $n = 20$. For 2D grating structures with an underlying Si film (Fig. 3.25c), convergence is achieved faster, i.e., for $n = 10$ at $\lambda \sim 1.0\ \mu\text{m}$. For all the calculations reported here, these numbers were used for absorption calculations.

Optical Absorption as a Function of Depth

Figure 3.27 plots optical absorption as a function of wavelength for three grating heights without (Fig. 3.25b) and with an underlying $5\text{-}\mu\text{m}$ -thick Si film (Fig. 3.25c). For both configurations, optical absorption increases rapidly for grating depth in $\sim 0\text{--}10\text{-}\mu\text{m}$ range. At larger depths between $15\ \mu\text{m}$ and $25\ \mu\text{m}$, absorption increase is slow. Overall optical absorption is slightly higher with underlying Si film. For these calculations, a $1.0\text{-}\mu\text{m}$ grating period with Si linewidth of $0.8\ \mu\text{m}$ was employed. Figure 3.28 plots the averaged optical absorption trend as a function of depth and linewidth. For calculations as a function of depth; linewidth of $0.8\ \mu\text{m}$ was used. Similarly, for absorption calculations as a function of linewidth, grating depth was kept fixed at $15\ \mu\text{m}$; for all calculations period was $1.0\ \mu\text{m}$.

Comparison of depth and linewidth measurements demonstrates the following trends:

- (i) Optical absorption increases rapidly for depths in 0- to $5\text{-}\mu\text{m}$ range.

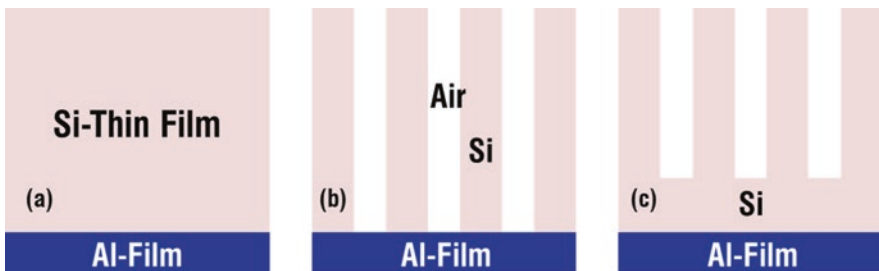


Fig. 3.25 Thin-film configurations used for optical absorption calculations

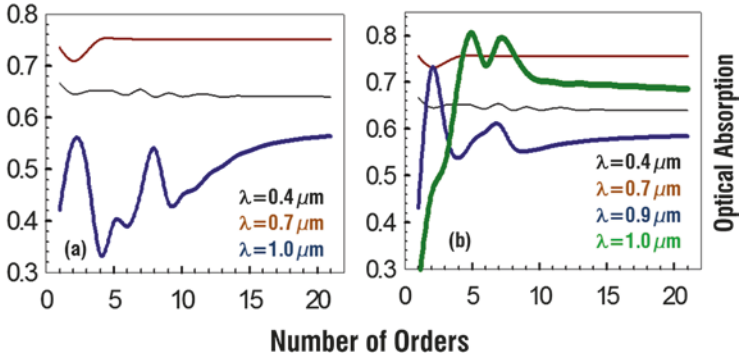


Fig. 3.26 Plot of optical absorption calculation convergence as a function of series summation index for two optical configurations: (a) Fig. 3.25b and (b) Fig. 3.25c

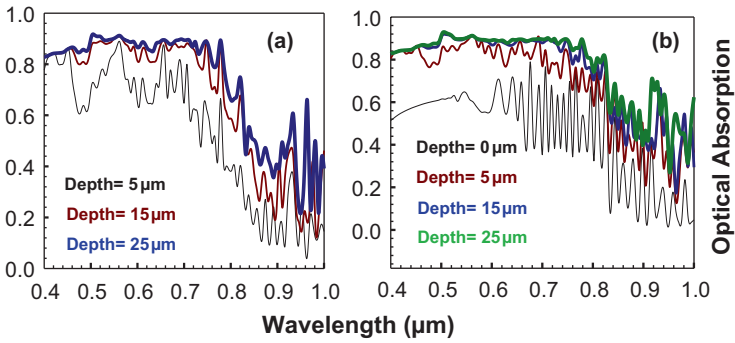


Fig. 3.27 Optical absorption as a function of wavelength for varying grating depths: (a) for configuration in Fig. 3.25b and (b) configuration in Fig. 3.25c

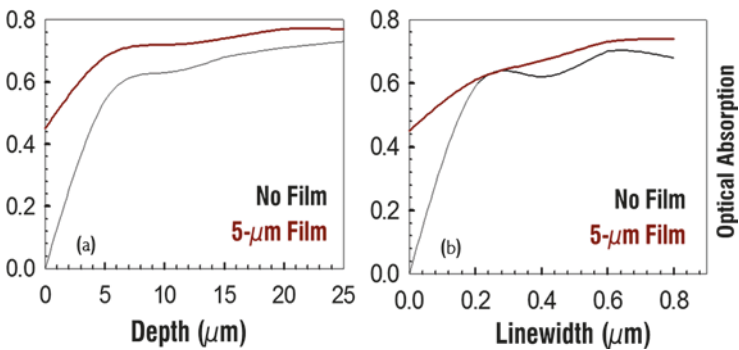


Fig. 3.28 Averaged optical absorptions plotted as a function of grating depth (a) and linewidth (b)

- (ii) Optical absorption remains relatively invariant in 5- to 25- μm range.
- (iii) Optical absorption with underlying film is slightly higher.
- (iv) Optical absorption increases rapidly with linewidth in 0–0.2- μm range, reaching near-maximum values at linewidths $\sim 0.6 \mu\text{m}$.

These simulations illustrate that grating depth in ~ 5 to 10- μm range may be sufficient to achieve complete optical absorption. This will mean substantial savings in Si material and etching costs.

Optical Absorption as a Function of Period

Figure 3.29 plots absorption as a function of wavelength for periods in 0.5- μm to 10.0- μm range. At 10- μm period, light interaction with periodic structures follows geometric optics with diffraction orders propagating nearly normal to the surface; lowest absorption is observed at this period. As period is reduced, absorption increases rapidly; highest absorption is achieved at 0.5- μm period. Comparison of four grating periods shows that the 0.8- μm period exhibits slightly higher absorption in 0.8–1.0- μm range.

Optical Absorption as a Function of Profile

Optical absorption dependence on surface profiles was investigated. Two-dimensional structures can either be in the form of post (Fig. 3.11b) or holes. Figure 3.30 plots optical absorption of post and hole patterns. For the same 0.4- μm Si linewidth, post patterns exhibit significantly higher absorptive response. Increase

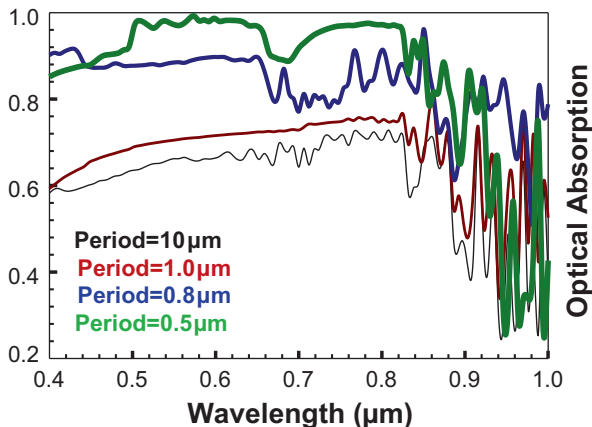


Fig. 3.29 Optical absorptions plotted as a function of wavelength for several grating periods with an underlying Si film of 5- μm thickness. Grating depth of 25 μm and linewidth of 0.8 μm were used for all calculations

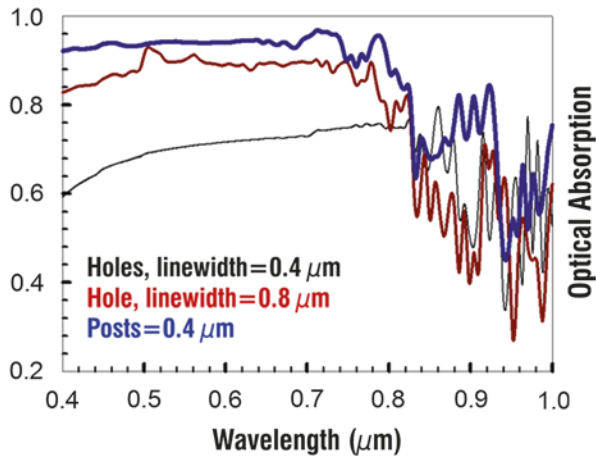


Fig. 3.30 Optical absorption in post and hole patterns plotted as a function of wavelength

in Si linewidth to $0.8 \mu\text{m}$ still leads to optical absorption lower than post pattern. In addition, the post pattern exhibits higher absorption in near-IR range. For these calculations, grating period was $1.0 \mu\text{m}$, and underlying Si thickness was $5 \mu\text{m}$ with grating depth of $25 \mu\text{m}$.

Summary of Optical Absorption Calculations

GSOLVER™ simulations of subwavelength periodic structures exhibit significant absorption enhancement in thin-film configurations. In order to compare optical absorption in 1D and 2D structures, optical absorption is plotted as a function of depth in Fig. 3.31 for three configurations in Fig. 3.25. The 2D grating structure exhibits rapid increase in absorption to a depth of $\sim 10 \mu\text{m}$; further increase in depth results only in slight absorption gain. For the composite structure, overall absorption for 2D structures is fairly independent of grating depth. In comparison with thin film only, the 2D gratings lead to $\sim 80\text{--}100\%$ increase in absorption, and $\sim 20\text{--}35\%$ increase relative to 1D gratings. The advantage of 2D gratings relative to 1D is better illustrated in Fig. 3.32 where optical absorption is plotted for the same period 1D and 2D gratings. For the 1D structure, the grating depth was $30 \mu\text{m}$ with an underlying $20\text{-}\mu\text{m}$ -thick Si film. For the 2D structure, the grating depth was $10 \mu\text{m}$ with an underlying $5\text{-}\mu\text{m}$ -thick Si film. Therefore, the optical absorption is significantly higher in a 2D structure in a total thickness less than $1/3$ of the 1D grating with an underlying thin film.

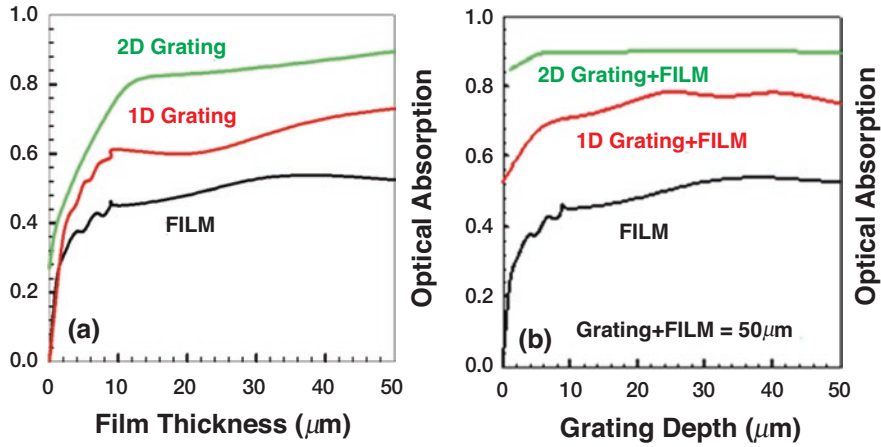


Fig. 3.31 Optical absorption plotted as a function of depth: (a) without an underlying film and (b) with underlying Si film on an Al substrate; also plotted optical absorption in 50- μm -thick Si film on an Al substrate

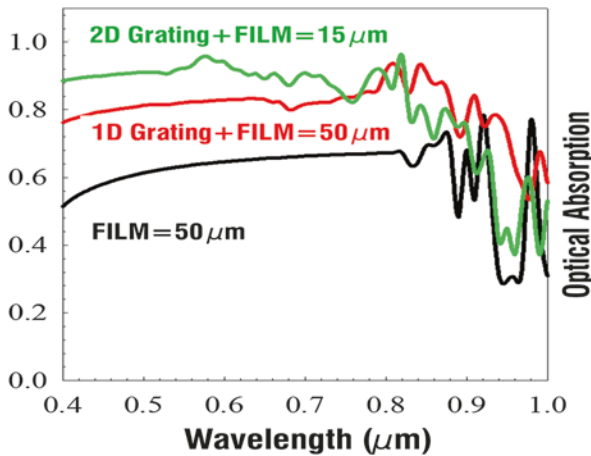


Fig. 3.32 Optical absorption plotted as a function of wavelength. Notice that for the 15- μm thickness with 2D grating structure, absorption is higher than the 50- μm -thick 1D grating structure; absorption in 50- μm -thick Si film on an Al substrate is also plotted for reference

3.6 Measured Optical Absorption in Thin Films

Experimental absorption measurements were carried out in 10- μm -thick silicon film in silicon-on-insulator (SOI) configuration [27]. Figure 3.33 illustrates three types of textured surfaces: randomly textured (Fig. 3.33a), 20- μm period 2D hole pattern etched to a depth of 10 μm (Fig. 3.33b), and 1- μm period 2D hole pattern etched to

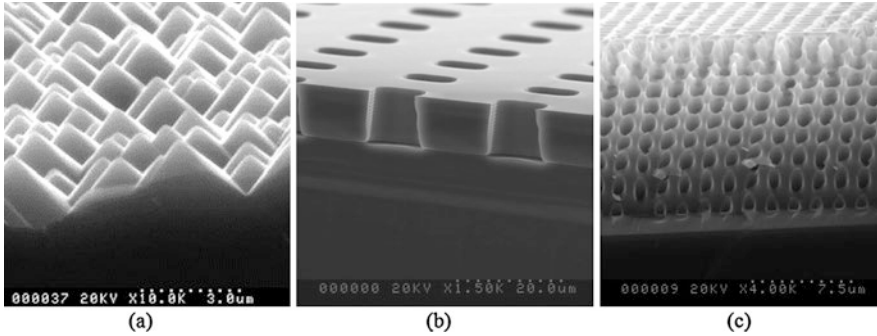


Fig. 3.33 SEM pictures of randomly textured subwavelength diffractive structures (a), 2D 20- μm period (b) and 2D 1- μm period (c) structures; all were etched to a depth of 10 μm in SOI configuration

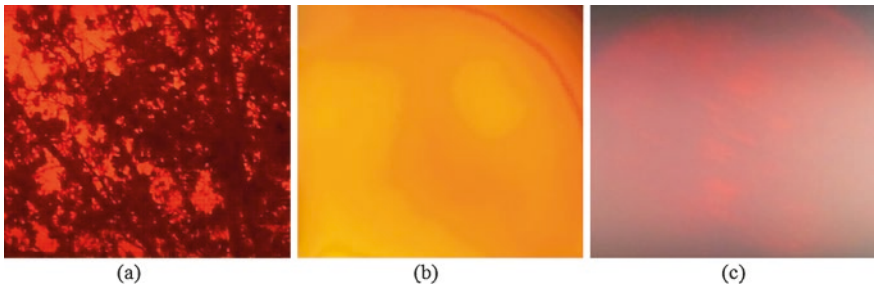


Fig. 3.34 Optical transmissions from 10- μm -thick Si films in planar (a), randomly textured (b), and periodically etched (c) configurations

a depth of 10- μm -thick Si in insulator (SOI) configuration. In order to determine optical absorption, planar and structured SOI substrates were attached to a glass slide followed by etching of Si substrate from the backside to the buried oxide layer. For optical absorption measurements, CCD camera and a monochromator-based optical system were employed for qualitative and quantitative absorption measurements. Figure 3.34 displays CCD images from planar (Fig. 3.34a), randomly textured (Fig. 3.34b), and 1- μm period, thru-etched (Fig. 3.34c) thin-film configurations. Salient features of identical CCD image with three SOI configurations at the entrance aperture are summarized below.

- (i) Orange transmission from planar, 10- μm -thick Si film.
- (ii) Translucent yellowish transmission from randomly textured 10- μm texture at the top surface of 10- μm -thick Si film (Fig. 3.33a).
- (iii) Weak coherent transmission from 1- μm period, 2D grating pattern etched to 10- μm thickness (Fig. 3.33c).

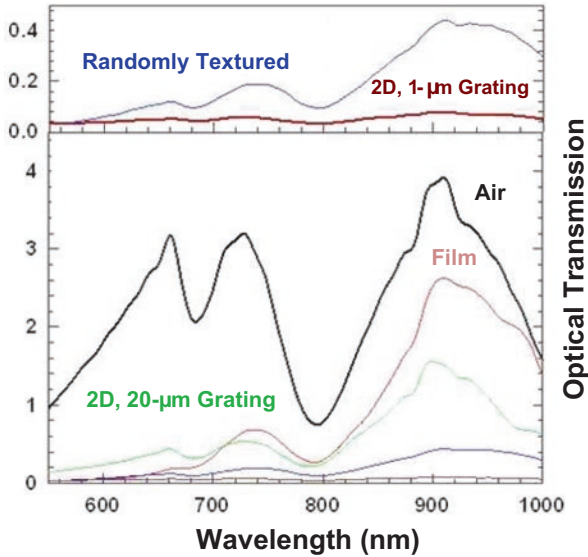


Fig. 3.35 Spectral transmission measurements from 10- μm -thick Si films in SOI configuration, planar (pink line), 20- μm period 2D grating (green line), randomly textured front surface (blue line), and 1- μm period 2D grating (brown line); for comparison system response in air is also plotted as black line

Figure 3.35 plots normal incidence spectral absorption measurements for these four optical transmission configurations; transmission in air has also been plotted for reference. For all absorption measurements, halogen light source was coupled to the entrance slit of a computer-controlled monochromator operating in $\lambda \sim 0.55\text{--}1.0\text{-}\mu\text{m}$ range. Output of the monochromator was focused onto a Si photodetector, which is plotted as a black line in Fig. 3.35, i.e., monochromator output in air. The artifacts at $\lambda \sim 0.68\ \mu\text{m}$, $\lambda = 0.8\ \mu\text{m}$, and $\lambda \sim 0.92\ \mu\text{m}$ are system related. Measurements of Si samples were carried out by placing them between the monochromator output and Si photodetector. Figure 3.35 plots absorption measurements from planar (pink line), Si film with 20- μm period 2D hole pattern (green line), front surface randomly textured (blue line), and 1- μm period 2D hole pattern (brown line); all films were of 10- μm thickness. The inset in Fig. 3.35 plots absorption of randomly textured and 2D, 1- μm period films at enlarged scale in order to identify spectral features. Principal features of absorption measurements have been summarized below.

- (i) Complete absorption for wavelengths below 600 nm except for 20- μm period.
- (ii) 20- μm period patterned film exhibits a transmission response similar to planar film except larger transmission in UV-visible range and slightly lower in IR range.
- (iii) Textured film exhibits broadband absorption.
- (iv) 1- μm period, 2D pattern exhibits the highest broadband absorption.

Optical absorption measurements are in good agreement with CCD images displayed in Fig. 3.34. Optical absorption is a function of light interactions based on geometrical, diffractive, and physical optics. Randomly textured subwavelength surface (Fig. 3.33a) creates a multiplicity of obliquely propagating transmitted diffraction orders inside thin Si film to completely randomize incident coherent image and also reduces transmission of normally propagating light. Deeply etched, 20- μm period grating pattern (Fig. 3.33b) interacts with light based on geometrical optics, and it maintains image coherence and transmits light below 600 nm on account of its hole pattern. Deeply etched 1- μm period, subwavelength structure exhibits the highest broadband absorption. These results are in good agreement with physical optics-based absorption in grating structures described above.

3.7 Reflection and Absorption in Randomly Textured Surfaces

Analysis of subwavelength periodic structures provides useful insights into light interactions with Si surface. However, cost considerations discourage applications of these structures in wafer-based solar cells; for thin films ($<15\ \mu\text{m}$), these are likely to prove beneficial. Randomly textured surfaces, described in Chap. 2, are ideally suited for solar cells. A randomly textured surface supporting subwavelength features is close approximation to a Lambertian surface. Lambertian analysis is based on random scattering in a weakly absorptive medium such as Si in the near-IR region where the effective optical absorption in a textured sheet (Fig. 3.36a) can be enhanced by as much as a factor of $4n^2$ relative to planar sheet, where n is the material refractive index. In the optical scheme described in Fig. 3.36b, the presence of random texture on sidewalls may be able to enhance absorption beyond the

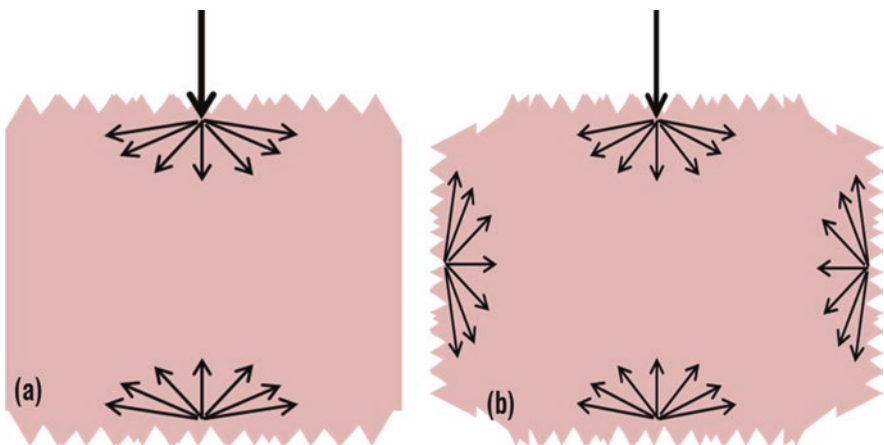


Fig. 3.36 Lambertian scattering within two parallel sheets (a) and within four sheets (b)

theoretical limit of $4n^2$ limit. This $4n^2$ absorption enhancement has the effect of improving the utilization of weakly absorbing photons near the band edge by the ratio of ~ 55 with $n \sim 3.7$ for Si. This also means that the cell thickness can be reduced by a factor of 55 while achieving the same absorption.

A randomly textured surface may be described by Fourier summation over a large number of periods. Diffractive scattering from this multiplicity of periodic structure ensures almost complete filling of the k-space. Angular distribution of light incident normally on a random surface follows diffraction equation given by

$$\theta_{m,i} = \sin^{-1} \frac{m\lambda}{nd_i}, \quad (3.12)$$

where $\theta_{m,i}$ represents propagation of m th diffraction order related to period, d_i , and n is refractive index. For example, if a random texture is formed by combining four periodic structures, the angular distribution of transmitted diffraction orders, calculated from Eq. 3.12, will be as shown in Table 3.1 for $\lambda = 1 \mu\text{m}$. As period increases, the number of diffraction orders increases with increasing angular separation. The fraction of energy coupled into each diffraction order is a complex function of several parameters including profiles and depths. Optical path length in geometrical optics is simply the sum of number of passes through a thin film of thickness t . In case of diffractive scattering, the optical path length for a single period is the sum over the propagating transmitted diffraction orders given by

$$L_{\text{OPL}}^{\text{grating}} = \sum_i \gamma_i l_i, \quad (3.13)$$

where γ_i is fraction of incident energy coupled into diffraction order length, l_i . For a normally propagating zero order, l_0 is identical to t , where t is the thickness of the wafer. For a diffraction order, the optical path is $t/\cos\theta_{m,i}$, where $\theta_{m,i}$ is the angle of propagation of the m th diffraction order corresponding to period, d_i . For a random subwavelength diffractive surface, the total optical path length is then summed over all grating periods (i), each of which generates diffraction orders (j) given by

$$L_{\text{OPL}}^{\text{random}} = \sum_{i,j} (\gamma_{i,j} l_{i,j}). \quad (3.14)$$

Equation 3.14 suggests substantial path length enhancement in suitably designed randomly textured surfaces in solar cells. Reducing reflection losses by a

Table 3.1 Angular distribution of transmitted diffraction orders inside Si

Grating period (μm)	(± 1) Orders (deg)	(± 2) Orders (deg)	(± 3) Orders (deg)	(± 4) Orders (deg)	(± 5) Orders (deg)
0.5	32.7	>90	>90	>90	>90
0.8	19.5	42.2	>90	>90	>90
1.0	15.8	32.7	54.2	>90	>90
1.5	10.5	21.2	32.7	46.1	65

mechanism that can simultaneously enhance its near-IR absorption is the key to boost solar cell efficiency [30]. Random RIE texturing methods offer the freedom to tailor reflection over a broad range. Figure 3.37 plots hemispherical reflectance as a function of wavelength for two textured surfaces; no AR films were applied to planar and textured surfaces. Scanning electron microscope profiles of textured surfaces in Fig. 3.38 reveal a broad distribution of linewidths, shapes, and depths. Texture-1 (Fig. 3.38a) dimensions are typically $\sim 1 \mu\text{m}$ with approximately cylindrical profiles. In contrast, texture-2 (Fig. 3.38b) supports linewidths in $\sim 50\text{--}300\text{-nm}$ range with depths in $\sim 100\text{--}500\text{-nm}$ range; profiles are approximately triangular. Similar to the behavior observed for periodic surfaces, reflectance reduction is a function of linewidths; nm-scale textures exhibit lower and μm -scale textures exhibit higher reflectance. Analysis below and solar cell data will clarify that structures with lowest reflectance are not necessarily the best for enhancing efficiency.

Fig. 3.37 Absolute hemispherical spectral reflectances plotted as a function of wavelength for textured surfaces; planar Si reflectance is also included for reference; no anti-reflection films were used

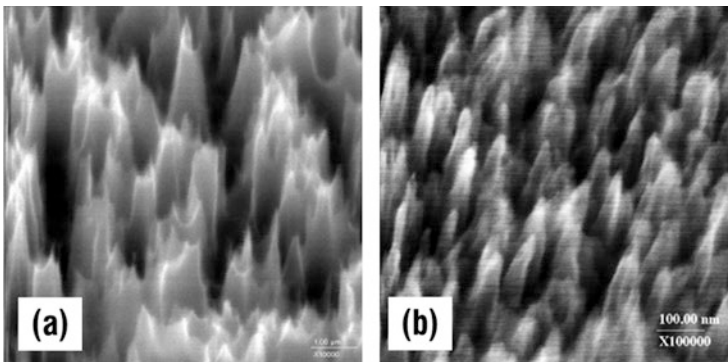
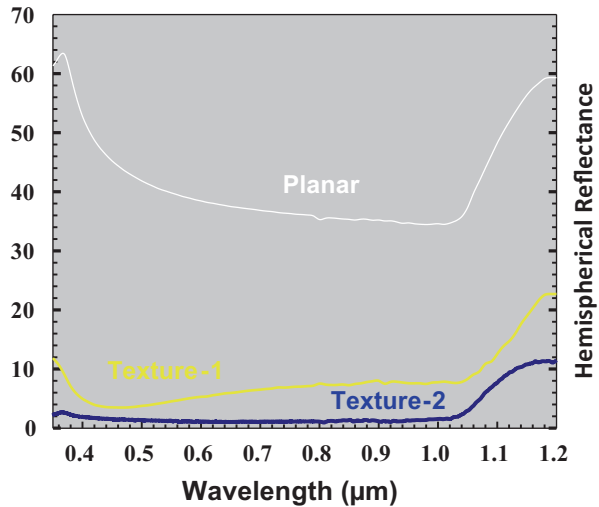


Fig. 3.38 Scanning electron microscope profiles of texture-1 (a) and texture-2 (b); SEM length scales are $1 \mu\text{m}$ for (a) and $0.1 \mu\text{m}$ for (b)

3.8 Fourier Analysis of Randomly Textured Surfaces

In randomly textured surfaces, it is difficult to extract meaningful information on spatial features. Fast Fourier transform (FFT) of randomly textured surfaces offers a way to measure spatial features of a given image [31]. In contrast with SEM image of the surface, its FFT generates a two-dimensional power spectrum. The power spectrum is the modulus of the Fourier transform. Peaks in the power spectrum represent the intensities of the frequency component in the data and appear as bright dots on a dark background and vice versa. Figure 3.39 displays atomic force images of two randomly textured surfaces. The FFT power images of the random surfaces in Fig. 3.39 are displayed in Fig. 3.40.

As a calibration exercise, FFT analysis was applied to 1D and 2D Si grating structures. The FFT power spectra images, of two 1D gratings in Fig. 3.41, are displayed in Fig. 3.42; their respective linescans are plotted in Fig. 3.43. It is noted that as the spatial period increases, the separation between the central term and primary peak decreases; the primary peak in the power spectra (Fig. 3.43) corresponds to the period of the grating.

Figure 3.44 plots hemispherical reflectance measurements from three textures defined by their SEM images and FFTs in Fig. 3.45. Lowest reflection is exhibited by texture C and highest by texture A. Figures 3.46 and 3.47 plot power spectra of all texture FFTs as a function of spatial frequency and period (Fig. 3.47). Texture C exhibits the most uniform distribution with dimensions in 1–3- μm range at full width at half maximum (FWHM); its spatial dimensions extend to $\sim 0.6 \mu\text{m}$. Texture B exhibits asymmetric size distribution in 1–5- μm range. Texture A exhibits a broad asymmetric maximum at $\sim 2.5 \mu\text{m}$; it has the largest spatial dimensions. Presence of finer features in textures B in comparison with texture C accounts for its slightly

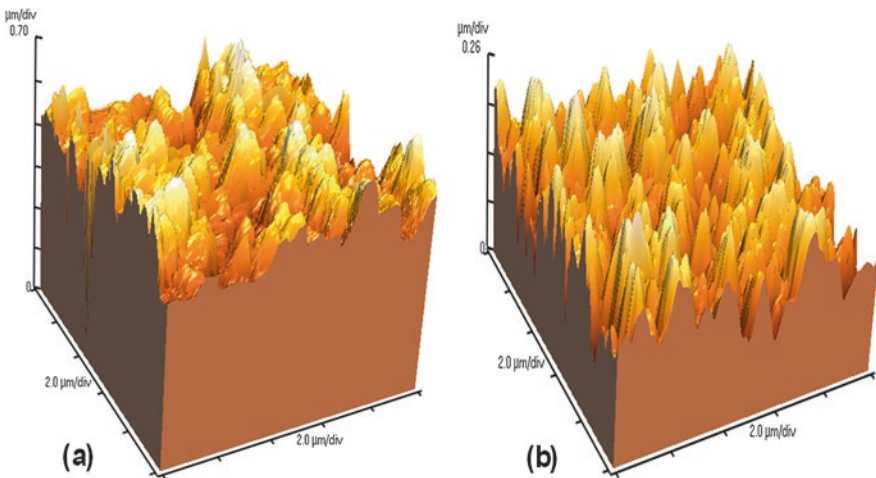


Fig. 3.39 Atomic force images of texture-1 (a) and texture-2 (b)

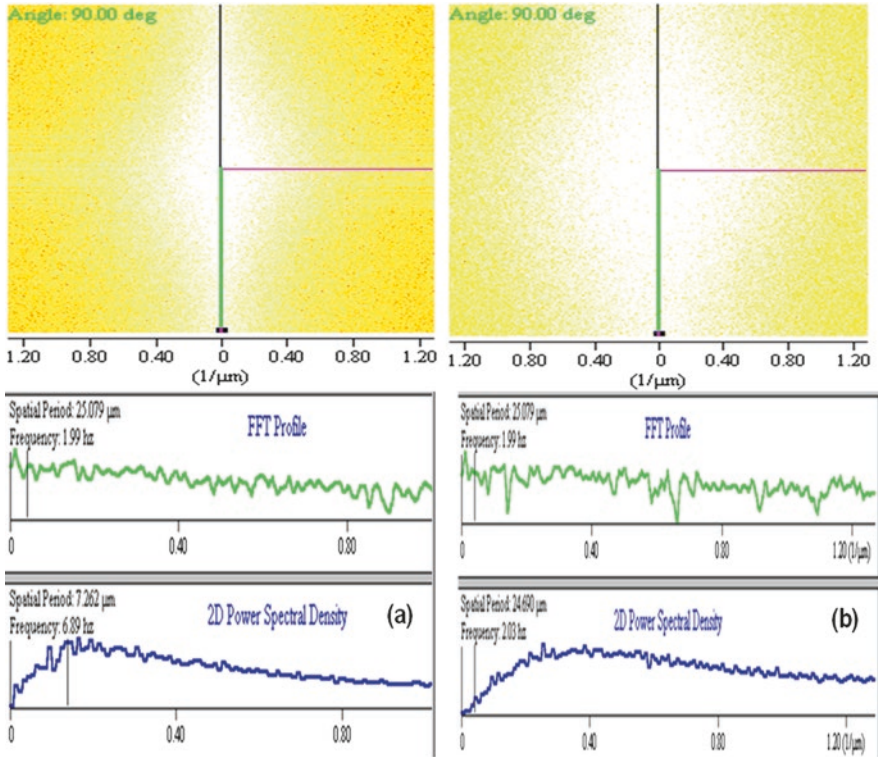


Fig. 3.40 Fast Fourier transforms, FFT profiles, and 2D power spectrum of texture-1 (a) and texture-2 (b)

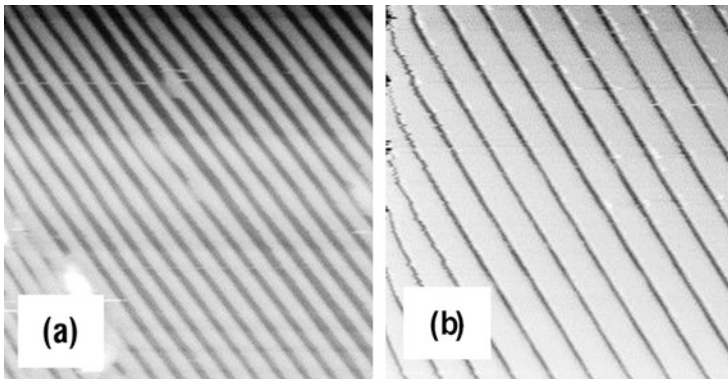


Fig. 3.41 Images of 0.27-μm (a) and 0.4-μm (b) period 1D Si grating structures

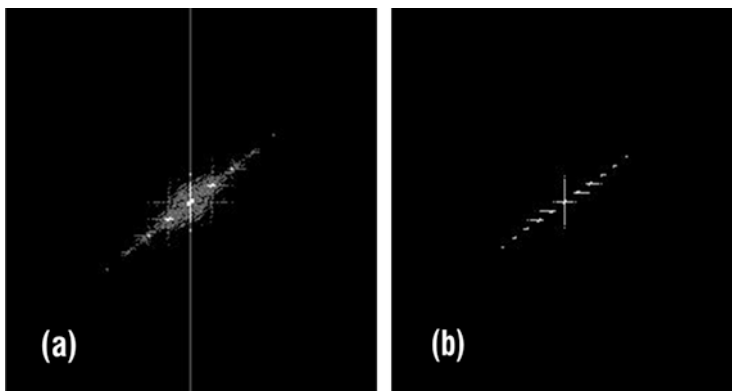


Fig. 3.42 FFT images of 0.27- μm period (a) and 0.4- μm period (b) 1D gratings

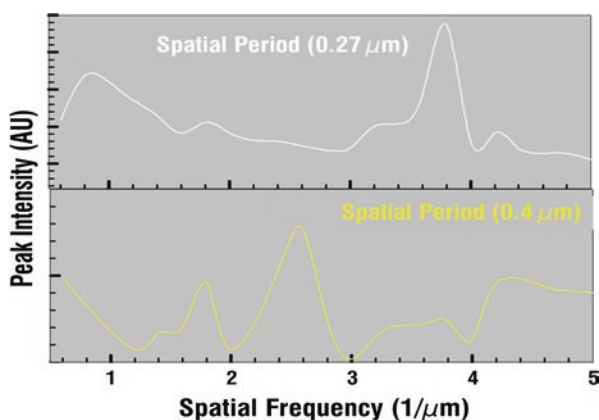


Fig. 3.43 Two-dimensional power density plots of the FFT images shown in Fig. 3.42

lower reflectance in short wavelength region. Presence of larger features in texture B results in higher reflectance than texture C in most of the visible region. Texture A exhibits larger features, hence its highest reflectance in UV-VIS region. All three textures have identical response in IR region. Higher reflectance in 1000–1200-nm spectral region is light above the bandgap.

3.9 Reflection and Absorption in 50-100- μm -Thick Films

Figure 3.48 plots hemispherical reflectance measurements from SiN-coated planar and randomly textured thin ($\sim 100 \mu\text{m}$) Si wafers. Averaged reflectance was $\sim 6\%$ for textured and 14% for planar surfaces, respectively. The textured surface exhibits lower reflectance in most of the spectral region. The textured wafer exhibits

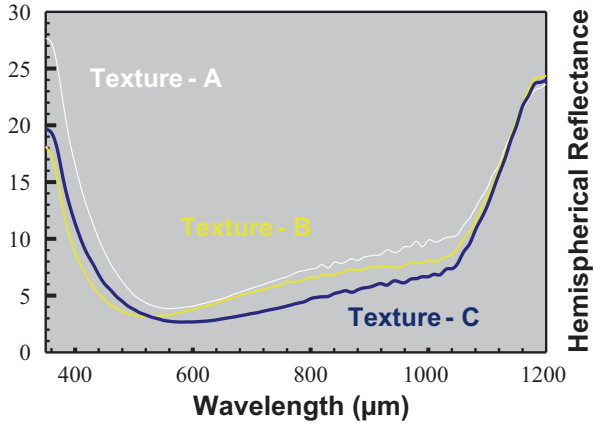


Fig. 3.44 Hemispherical reflectance measurements plotted as a function of wavelengths for three randomly textured surfaces; all surfaces were coated with SiN film

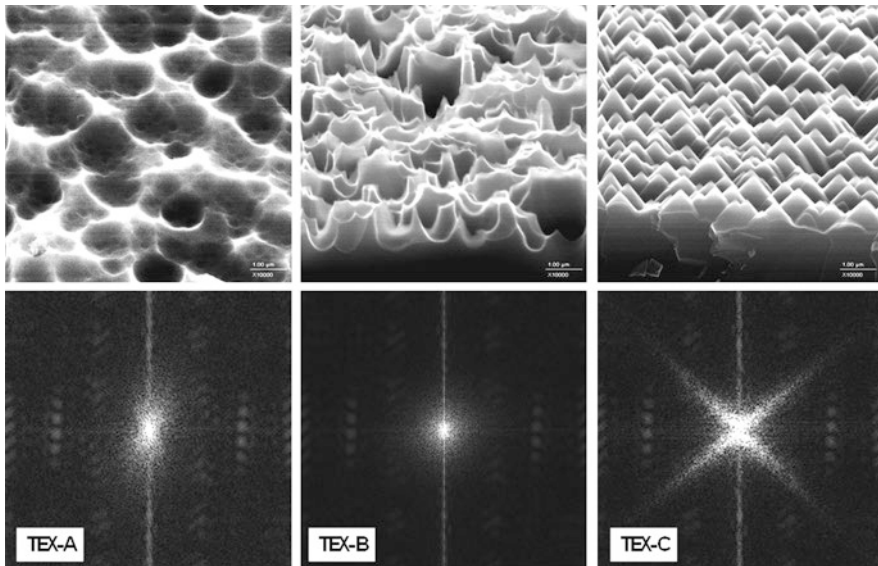


Fig. 3.45 SEMs and FFTs of profiles of three textures in Fig. 3.44: (a) Texture A, (b) Texture B, and (c) Texture C

substantially higher absorption in the IR region. Solar cell performance from this texture will be presented in Chaps. 5 and 6.

Figure 3.49 displays hemispherical reflectance measurements from 25- to 50- μm -thin planar (Fig. 3.49a)-textured (Fig. 3.49b) films [28]. SEM profiles of the textured surfaces in Fig. 3.49c reveal distribution of surface features in $\sim 0.5\text{--}2.0\text{-}\mu\text{m}$ range. The vertical scale for both the planar and textured measurements is the same.

Fig. 3.46 Two-dimensional power spectra of FFT images in Fig. 3.45

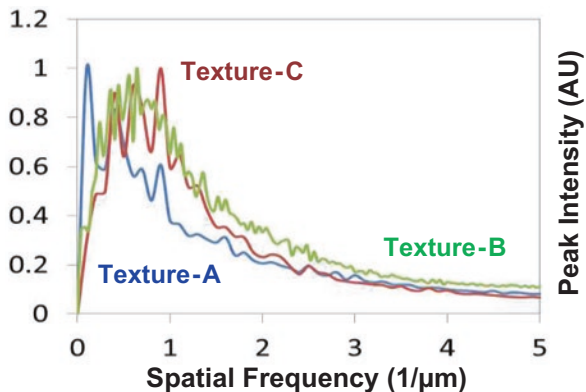
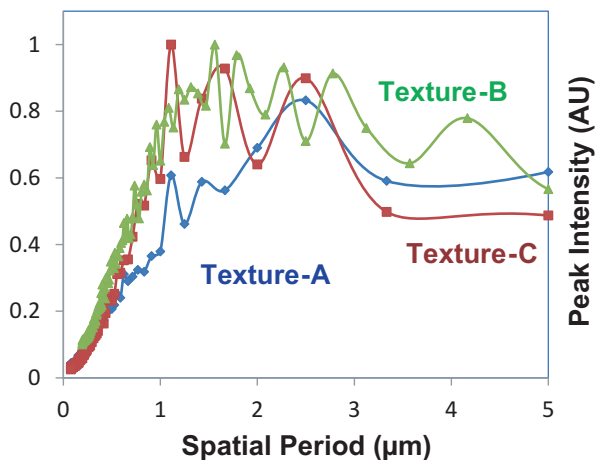


Fig. 3.47 Two-dimensional power spectrum of FFT images in Fig. 3.45 plotted as a function of spatial periods



Reflection reduction by ~ 1000 is observed in UV-VIS-NIR regions. It is noted that for the 25- μm -thick Si films, most of the light is reflected in ~ 1000 – 1200 -nm spectral region where Si absorption becomes almost zero. The same behavior is not observed from 50- μm -thick films. This is attributed to the substrate bulk doping variations. The substrate for 25- μm films was from lightly (~ 5 ohm-cm) boron-doped Si, while 50- μm -thick film was from heavily doped (~ 0.002 ohm-cm) Si wafer. Almost 100% absorption has been achieved even for 25- μm -thick film.

3.10 Optical Transmission

Hemispherical reflection measurements provide reflectance information through most of the UV-VIS-IR region; however, there is insufficient information near the bandgap where the texture impact is most critical. Most of the incident light is

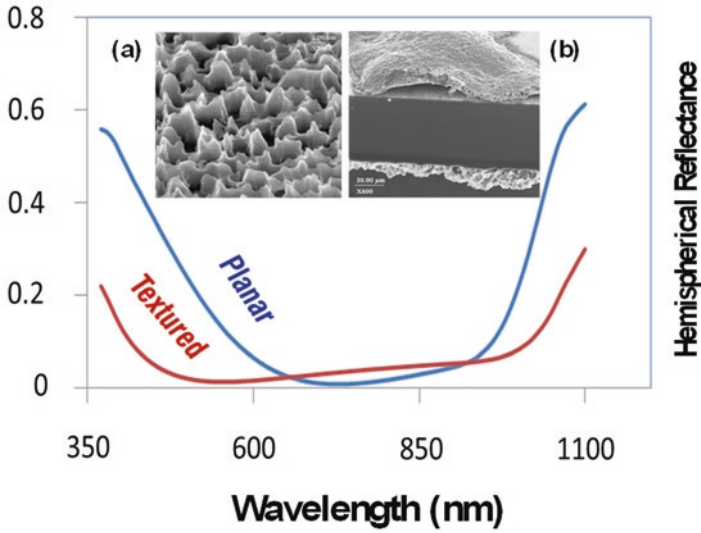


Fig. 3.48 Hemispherical reflection in 100- μm -thick n-type c-Si films; backside was metallized with thermally annealed Al paste; inset shows SEM pictures of the textured surface and completed solar cell with top Ag and bottom Al-cured screen-printed contacts

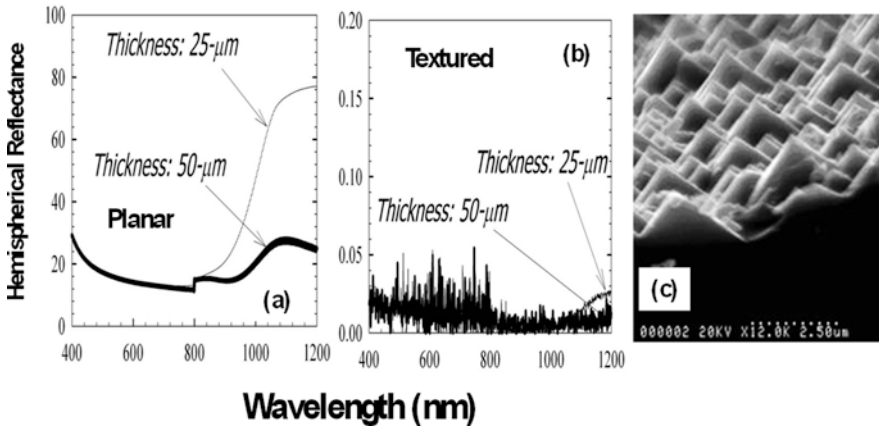


Fig. 3.49 Hemispherical reflectance measurements plotted versus wavelength for planar (a) and textured (b) films, also shown is microstructure of the textured surface (c)

absorbed in Si for wavelengths less than 900 nm. At longer wavelengths, light absorption is weak and texture plays a critical role. Figure 3.50 describes system schematic for spectral transmission measurements over broad spectral range [32]. Optical transmission system is based on computer-controlled diffraction grating in 750–1600-nm spectral range. Transmitted light passes through sample and is collected by an InGaAs photodetector. In a typical measurement, transmitted signal is

Fig. 3.50 Optical transmission measurement system schematic as a function of wavelength

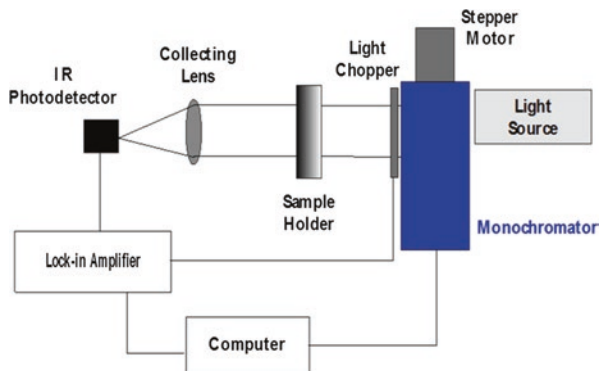
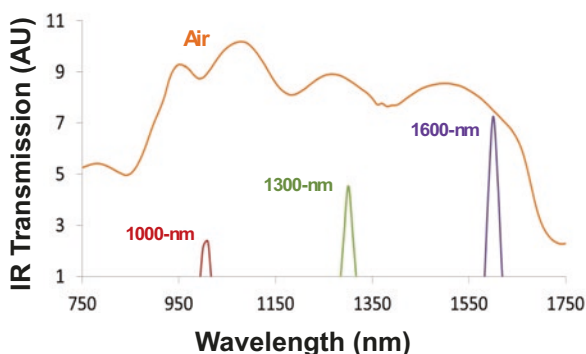


Fig. 3.51 Calibration response of spectral transmission system as a function of wavelength for three calibrated narrowband filters



measured as a function of wavelength; relative calibration is provided by comparison with transmission in air and through sample. Transmission through a wafer will be a function of its texture and bulk resistivity. Figure 3.51 plots transmission measurement in air and through calibrated narrowband optical filters. The peak transmission wavelengths are in excellent agreement with filter specifications. This system was used to investigate transmission through Si wafers with varying textures and AR films. Figure 3.52a plots spectral transmission from planar (SiO_2/Si) and textured ($\text{SiN}/\text{mc-Si}$) wafers as a function of wavelength in 750–1200-nm range. The transmission signal variation has been plotted on logarithmic scale. Textured surface transmission is observed to be significantly lower than planar surface across the entire wavelength range. The textured surface profile, illustrated in Fig. 3.52b, exhibits large ($\sim 2\text{--}5\ \mu\text{m}$) features typical of nitric acid-based texturing.

Figure 3.53 plots spectral transmission from textured surfaces, i.e., wet-chemically textured surface with minimal reflectance (black Si) and $\text{SiN}/\text{mc-Si}$ surface; transmitted data has been plotted on both linear and logarithmic scales. The transmission through black Si surface is significantly lower than the $\text{SiN}/\text{mc-Si}$ surface. This is better illustrated in Fig. 3.54 by plotting the ratio of the transmission signal from the two wafers. The transmission in black Si is reduced by a factor of ~ 10 at 1000 nm, ~ 40 at 1200 nm, and ~ 100 at 1600 nm. The black Si has been wet-chemically textured with surface features similar to those illustrated in Figs. 3.45c

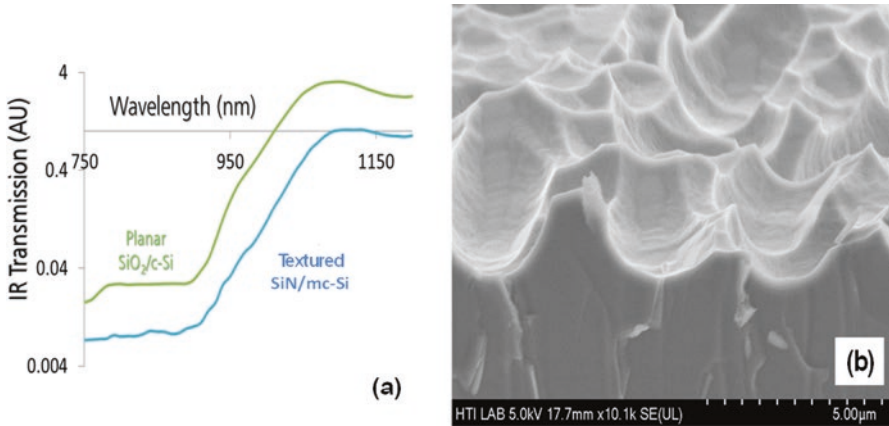


Fig. 3.52 Transmission response of planar and textured Si wafers plotted as a function of wavelength

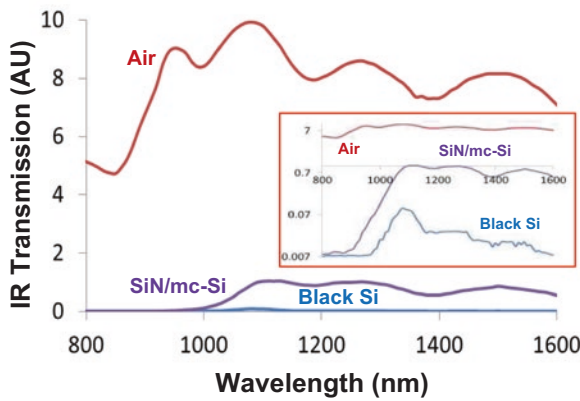


Fig. 3.53 Optical transmission comparison as a function of wavelength for SiN- and SiO₂-coated textured wafers

and 3.49c; hence, diffractive coupling based on pyramidal features is far more effective than the acidic texture.

3.11 Lifetime and Surface Recombination Velocity Characterization

Limiting efficiency of a solar cell is largely determined by two wafer parameters: bulk lifetime and surface recombination velocity [33]. Software simulations in Chap. 1 illustrated sensitive dependence on lifetime and surface passivation in order

Fig. 3.54 Ratio of optical transmission plotted as a function of wavelength for SiN- and SiO₂-coated wafers

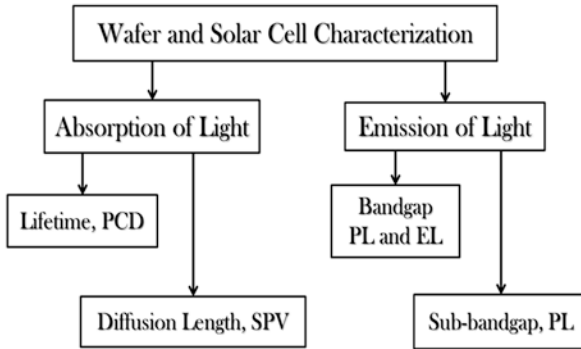
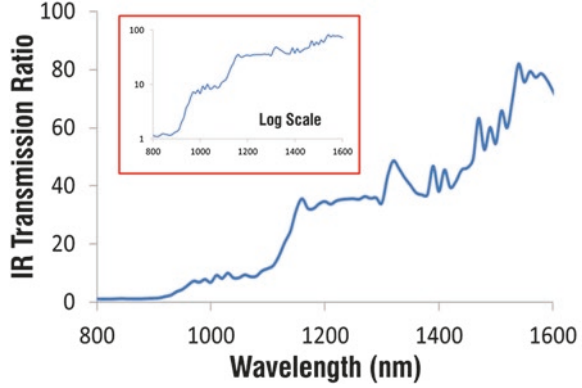


Fig. 3.55 Physical mechanisms for wafer and solar cell characterization approaches aimed at evaluation of lifetime and surface recombination velocity

to achieve efficiency consistent with wafer specifications. Generally available methods for lifetime and surface recombination velocity measurements are described in Fig. 3.55. Response of either the wafer or solar cell is determined by studying its absorption or conversely emission of light. Response to absorption is a function of physical characteristics of incident light including temporal, spectral, and intensity parameters. With pulse light sources such as lasers or flash lamps, transient photoconductive decay (PCD) response of the semiconductor response is measured to calculate its lifetime. In case of steady-state light sources, surface photovoltage (SPV) of the semiconductor is measured to calculate its minority carrier diffusion length.

Emission of light is broadly characterized into two categories: bandgap and sub-bandgap. Bandgap is light emitted by semiconductor, i.e., it photoluminescence, based on its characteristic bandgap value (1.13 μm for Si). Sub-bandgap radiation is a function of impurity-based defects. Typical PL measurement requires excitation in either steady-state or pulse mode and detection of emitted light with charge coupled

device (CCD) cameras. These methods allow large-area spatial mapping; however, significant signal processing is needed in order to extract meaningful information. The electroluminescence (EL) measurement is based on forward-biased electrical excitation of the semiconductor device. In Si solar cells, current densities are typical of its operation under sunlight.

All of these methods are generally effective with respective strengths and weaknesses. As a general rule, practice of any given method is a function of several conditions including cost, speed, expertise, and need. In view of author's expertise in SPV instrumentation, SPV analysis, supported with experimental data, is presented for silicon wafers as a function of texture and surface states. Adequate background with relevant references is provided for all other methods.

3.11.1 Photoconductive Decay Method

Exponential decay of photo-generated excess carriers in a semiconductor is given by

$$n(t) = n_0 \exp(-t / t_{\text{eff}}), \quad (3.15)$$

where n_0 is carrier concentration at $t = 0$ and t_{eff} is defined by

$$1 / t_{\text{eff}} = 1 / t_B + D\beta^2, \quad (3.16)$$

where t_B is the bulk lifetime and relationship of β to D and temperature T is given by

$$\beta \tan(\beta T / 2) = S_r / D, \quad (3.17)$$

where D is the diffusion coefficient and S_r is surface recombination velocity; for detailed mathematical formalism, please see references for background [34–38]. Equation 3.16 reveals that the measured lifetime in a semiconductor is a combination of bulk lifetime and surface recombination velocity-based time constant. Therefore, this method would work particularly well for (a) short lifetime for which excess carriers recombine before reaching the surface and (b) negligible surface recombination velocity. The first condition eliminates surfaces and, if that is not possible, the second condition ensures high-quality surface passivation.

Lifetime measurement in photoconductive decay (PCD) method is based on measuring photoconductive transient response (Fig. 3.56). As laser-generated excess carriers diffuse to the surface, photoconductive-based reflection modulation is detected with microwave signal. Measurement resolution limits are established by microwave equipment and incident pulsed laser. A variation of this method is quasi-state photoconductance in which laser is replaced by flash lamp with pulse duration in millisecond range. This method is able to measure lifetime over a broad range.

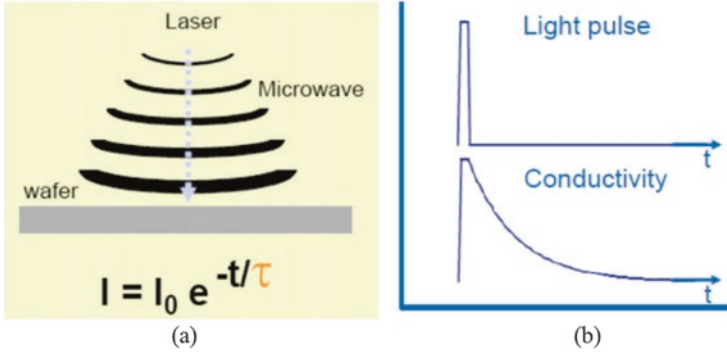


Fig. 3.56 Photoconductive approach to lifetime measurement with incident pulsed radiation on semiconductor wafer coupled to the microwave cavity (a) and its transient conductivity variation with time to measure lifetime (b)

3.11.2 Surface Photovoltage Method

Surface photovoltage (SPV) method is based on Goodman's formalism developed for diffusion length measurements in semiconductors [39]. Light incident on a semiconductor creates electron-hole pairs, which diffuse to the surface under the influence of electric field due to depletion region at the surface. The presence of these excess carriers in the depletion region at the surface creates the surface photovoltage effect. The distance excess minority carrier travel before recombination is the diffusion length. The surface photovoltage method works under steady-state conditions to measure minority carrier diffusion lengths at injection levels that are five to six orders of magnitude lower than PCD. A detailed description of SPV formalism has been provided in references [40–45].

Exponential absorption of incident light inside a semiconductor is given by

$$\phi(x) = \phi_{\text{eff}} e^{-\alpha x}, \quad (3.18)$$

where α is the absorption coefficient of the semiconductor and ϕ_{eff} is given by

$$\phi_{\text{eff}} = (1 - R)\eta\phi_0, \quad (3.19)$$

where R is the surface reflectance, η is the quantum efficiency, and ϕ_0 is the photon flux at the semiconductor surface. In order to apply Goodman's SPV model to p-type semiconductor with hole density p , electron density n , excess carrier density Δn , wafer thickness t , depletion length width L_w , and diffusion length L_d , the following conditions must be satisfied:

- (i) $p \gg n$
- (ii) $p \gg \Delta n$
- (iii) $t \gg 1/\alpha \gg L_w$
- (iv) $t \gg L_d \gg L_w$

Under these conditions, the relationship between photon flux and surface photovoltage is given by

$$\phi_{\text{eff}} / V_{\text{SPV}} \propto L_d + 1/\alpha. \tag{3.20}$$

A plot of $\phi_{\text{eff}}/V_{\text{SPV}}$ versus $1/\alpha$ in Eq. 3.20 will intersect at $x = -L_d =$, i.e., the diffusion length of the semiconductor. Given the resistivity of the semiconductor, the minority lifetime τ is determined by the relationship

$$\tau = Ld^2 / D, \tag{3.21}$$

where D is the diffusion coefficient of the semiconductor.

Surface photovoltage, V_{SPV} , is measured by two methods: method A, or the constant voltage approach, in which ϕ_{eff} is measured at constant V_{SPV} , and method B, in which ΔV_{SPV} is measured as a function of $1/\alpha$ at constant flux. Method B has been extensively used due to its faster data acquisition and simplicity since once calibrated, no further flux measurements are required. Figure 3.57a plots absorption depth in Si as a function of wavelength [1]. It is noted that Si exhibits strong absorption through most of the UV-near-IR region. As wavelengths approach closer to the bandgap, light absorption is poor requiring large wafer thicknesses to achieve complete absorption. In practice, $1/V_{\text{SPV}}$ is experimentally measured as a function of wavelength at constant flux and plotted as a function of $1/\alpha$ as described in Fig. 3.57a. At longer wavelengths, absorption depth increases, while V_{SPV} decreases due to longer diffusion lengths, resulting linear response is curve-fitted, and the graph intersection at $x = 0$ yields minority carrier diffusion length.

AFORS-HET numerical software for solar cell and measurements has been used to simulate V_{SPV} as a function of wavelength [46]. Figures 3.58, 3.59 and 3.60 display software screens and wafer configurations employed for calculations. The main screen (Fig. 3.58a) describes all the available calculation options; only

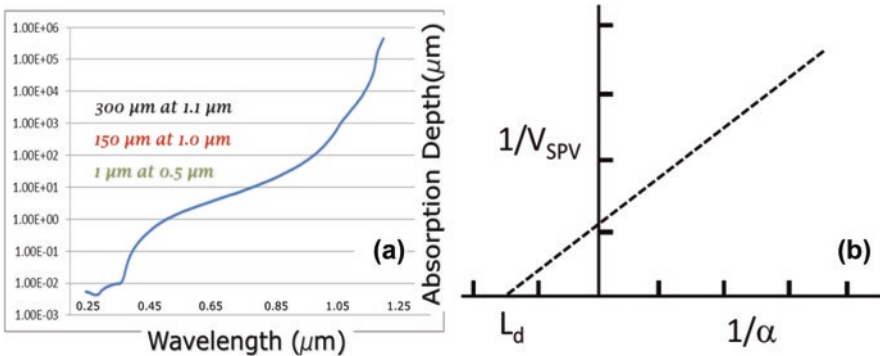


Fig. 3.57 Plot of light absorption depth in Si as a function of wavelength (a) and determination of diffusion by plotting $1/V_{\text{SPV}}$ as a function of $1/\alpha$ (b); intersection of the graph at the x -axis yields L_d

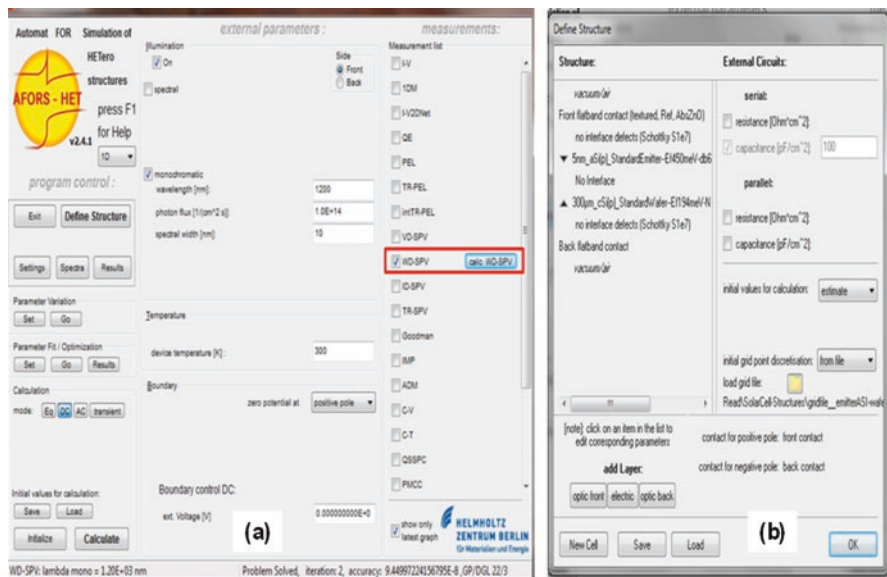


Fig. 3.58 Main software screen in AFORS-HET simulations displaying a wide range of options, wavelength-dependent V_{SPV} which has been identified by a red border (a) and the software screen describing wafer configuration calculations (b)

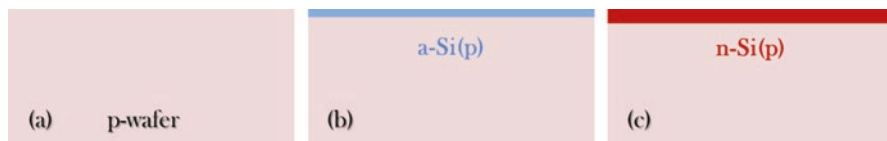


Fig. 3.59 Wafer configurations investigated for V_{SPV} simulations: (a) p-wafer (a), (b) a-Si/p-Si, and (c) n/p wafer

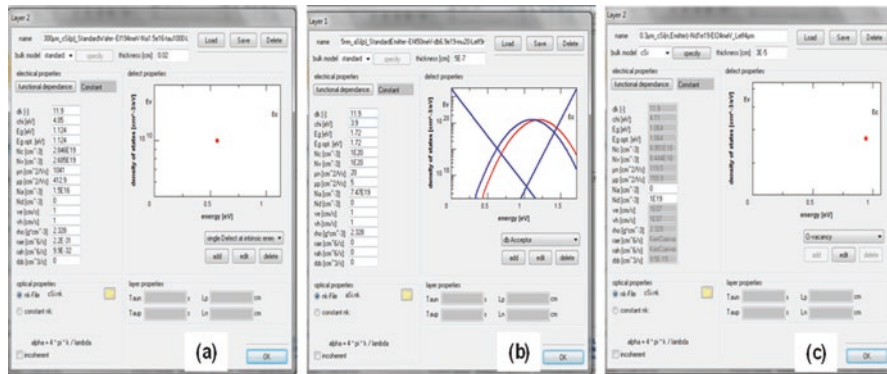


Fig. 3.60 Doping profiles and bandgaps for three measurement configurations in Fig. 3.59: p-wafer (a), a-Si(p) layer on p-Si wafer, and n-diffused layer on p wafer (c)

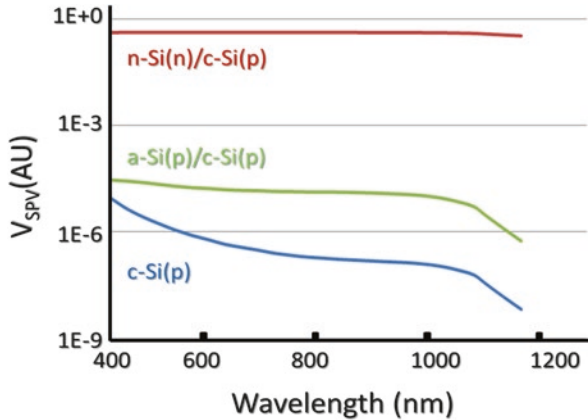


Fig. 3.61 Surface photovoltage variation as a function of wavelength for surface variations described in Figs. 3.59 and 3.60; for all the simulations, wafer doping was $1.5E16$ and recombination velocity was 1 cm/s

wavelength-dependent option, highlighted by a red border, was selected. Wafer configurations chosen for V_{SPV} calculations, as described in Fig. 3.59, are meant to exhibit its sensitivity as a function of surface and bulk parameters. Figure 3.60 describes material parameters for Si (p) wafer (Fig. 3.60a), a-Si(p) surface passivation layer (Fig. 3.60b), and n-Si emitter layer (Fig. 3.60c). Based on these parameters, V_{SPV} variation as a function of wavelength is plotted in Fig. 3.61 for all three configurations; logarithmic scale has been used for V_{SPV} . It is noted that V_{SPV} signal is extremely sensitive to surface conditions exhibiting several orders of magnitude variation as a-Si(p) and n-emitter layers are added to the front surface of Si(p) wafer. The V_{SPV} response as a function of wavelength is relatively flat in UV-VIS spectral regions and decreases rapidly for wavelengths reaching Si bandgap. The simulations in Fig. 3.61 reveal extreme sensitivity of the SPV method to surface conditions. Figure 3.62 plots V_{SPV} variation as a function of wafer doping level for three wavelengths in VIS-IR range. V_{SPV} signal decreases in logarithmic manner at high doping levels; typical solar cell wafers have a doping level of $\sim 1.5E16$ cm^{-3} range. Wafer doping level is related to lifetime [34]; therefore, V_{SPV} variation is indirectly related to lifetime by plotting V_{SPV} as a function of lifetime in Fig. 3.63. It is noted that V_{SPV} increases linearly with lifetime at lower values and saturates at large lifetime values; wafers used for high-efficiency back-contact solar cells require lifetimes ~ 1000 – 10000 μs . These AFORS simulations of SPV reaffirm sensitivity of the approach to surface passivation and lifetime.

3.11.3 Bandgap Photo- and Electroluminescence Methods

Crystalline Si is an indirect bandgap semiconductor with bandgap at 1150 nm; its bandgap emission efficiency is poor and strongly dependent on surface passivation and lifetime. Spatially resolved bandgap photoluminescence (PL) has long been

Fig. 3.62 Surface photovoltage variation plotted as a function of doping level for three different wavelengths

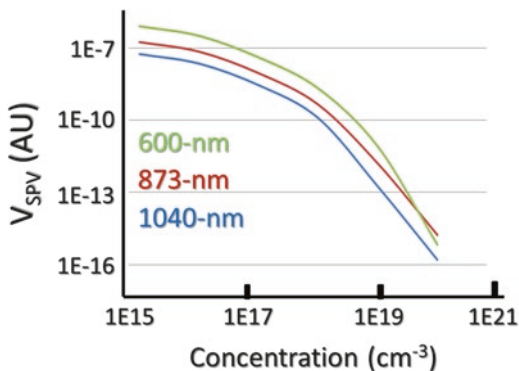
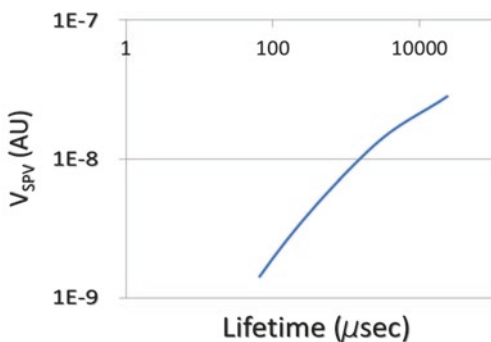


Fig. 3.63 Surface photovoltage intensity variation plotted as function of lifetime



identified by researchers as a reliable process monitoring tool in photovoltaics research [47–53]. With the advent of advanced charge coupled device (CCD) cameras based on Si and InGaAs combined with advanced real-time image processing, spatial PL imaging has become an important process characterization instrument for silicon wafers and solar cells. Assuming negligible absorption within Si, PL intensity is a function of photo-generated electron-hole pairs across wafer thickness given by

$$I_{\text{PL}} \cong C \cdot N_{\text{D}} \cdot \Delta n, \tag{3.22}$$

where C is the process-dependent constant, N_{D} is the doping concentration, and Δn is the local minority carrier concentration [54]. Under steady-state excitation conditions, the effective minority carrier lifetime is determined by

$$\tau_{\text{eff}} \cong \Delta n / G, \tag{3.23}$$

where G is the average minority carrier generation per unit volume. In a typical PL image from a single or multicrystalline Si wafer; intensity fluctuations reflect spatial surface defects. If instead of optical excitation, solar cell is electrically excited, i.e.,

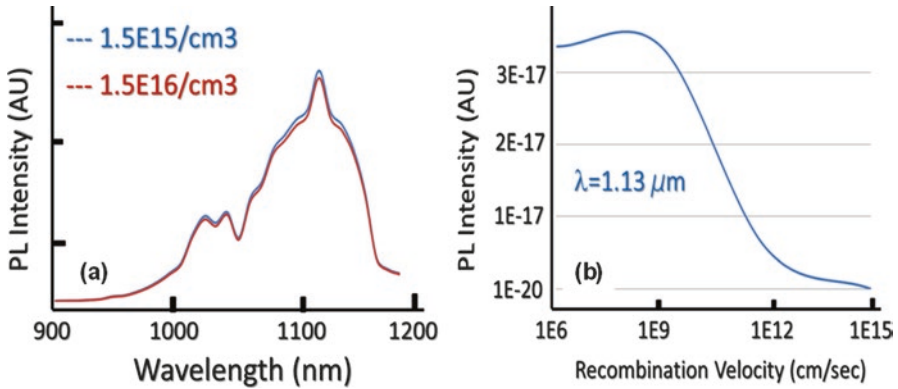


Fig. 3.64 PL intensity variation with (a) doping and (b) surface recombination velocity (b)

solar cell operating in forward bias, it also emits radiation at its bandgap known as electroluminescence (EL) [55]. This EL radiation is measured using either cooled Si CCD or InGaAs CCD cameras to provide both spectral and spatial information. Images of EL from a Si solar cell are acquired under forward bias at 40 mA/cm^2 current density, which is close to the actual operation of the solar cell under sunny conditions [56–58].

AFORS-HET software has been used to evaluate PL efficiency as a function of wafer parameters. Figure 3.64a plots PL signal for two p-type wafer densities with insignificant variation. At higher doping levels, PL signal is not detectable. Figure 3.64b plots PL signal intensity as a function of surface recombination velocity. There is insignificant variation in PL intensity for low recombination velocities (up to $\sim 1E7$ cm/s); however, at higher recombination velocities, signal rapidly decreases by three orders of magnitude. PL signal measurements require sensitive CCD cameras and are generally more applicable to high lifetime wafers.

3.11.4 Sub-band Photoluminescence

In addition to bandgap imaging, wafer lifetime is also characterized by detecting sub-bandgap emissions in $\sim 1.3\text{--}25\text{-}\mu\text{m}$ range. In the transient approach, incident pulsed laser and its transient response is detected to determine lifetime and recombination velocity. Infrared lifetime imaging (ILM) is a steady-state approach in which transmission of IR light is measured in response to bandgap excitation; this method is also known as carrier density imaging. In this approach, optical excitation changes absorption coefficient which is detected either in transient or steady-state modes to determine lifetime [59–61].

3.12 Diffusion Length Measurements with Surface Photovoltage

In this section, application of surface voltage method to determine diffusion lengths and lifetimes will be presented starting with experimental configuration, extraction of diffusion length from experimental data, measurement resolution, and a quantitative evaluation of surface recombination velocity.

3.12.1 Experimental Apparatus

Figure 3.65 describes experimental configuration devised for surface photovoltage measurements. Light from a quartz halogen lamp is collimated to pass through a stepper-motor-controlled monochromator operating in 400–1200-nm spectral range [62]. Spectrally distributed light output from the monochromator passes through an optical chopper and is incident on the wafer using a folding mirror. The wafer is placed on Au-plated wafer holder with an Au-ITO/quartz plate on its top side. The surface photovoltage is detected capacitively using lock-in amplifier which uses as input the V_{SPV} signal from the wafer assembly, reference from the chopper is connected to the lock-in amplifier, and its output is connected to the computer. The entire assembly is placed in a black box. The surface photovoltage is measured as a function of wavelength using LabVIEW-based control software.

This system allows SPV measurements in UV-VIS-IR spectral regions. Measurements in UV (~400–500 nm) region are useful for evaluation of surface effects including surface recombination velocity; measurements in visible region are comparatively less sensitive. For diffusion length measurements, spectral range

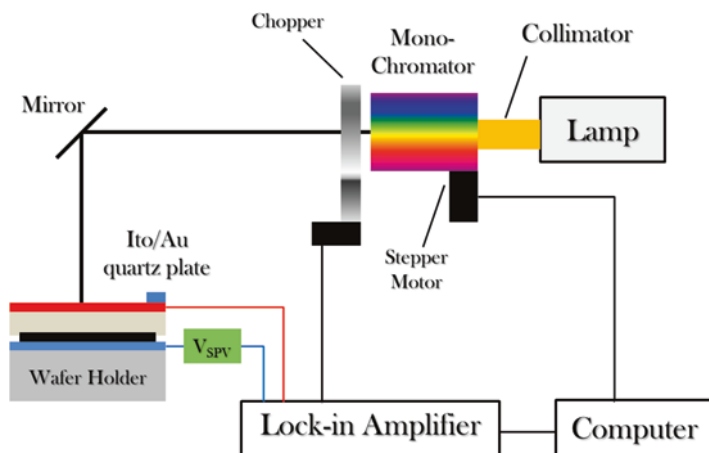


Fig. 3.65 Experimental configuration designed for surface photovoltage measurements

in 950–1050-nm region, with absorption depths in ~64–600- μm range, was selected to minimize impact of surface defects. In this 100-nm wavelength range, photon flux is assumed to be constant.

3.12.2 Surface Photovoltage Measurements on Silicon Wafers

Figure 3.66 describes measurement methodology. Surface photovoltage is measured in 950–1050-nm spectral range, absorption depth for this wavelength range is used from literature [1], and $1/\alpha$ is plotted versus $1/V_{\text{SPV}}$. A linear squares fit is applied to the measured data, and L_d is given by intersection of the graph at $y = 0$; for diffusion length measurements, R^2 was in 0.98–0.99 range. With measured diffusion length, L_d , for known wafer resistivity, minority carrier lifetime, τ , is calculated from Eq. 3.21; plot of τ as a function of L_d in Fig. 3.67 for wafer diffusivity of $27 \text{ cm}^2/\text{s}$ exhibits linear response. For relatively low lifetime wafers in ~10–20- μsec range, diffusion lengths are in ~170–230- μm range.

In the low-injection regime, V_{SPV} varies over a wide range measurable with the lock-in amplifier. Figure 3.68 plots measured V_{SPV} signal for lock-in scale in 1- μV to 10-mV range; below 1- μV signal was noisy. The V_{SPV} measurements were consistent over almost five orders of magnitude indicating sensitivity of this method; signal variation is largely attributed to lifetime and surface passivation. In order to evaluate dependence of diffusion length on SPV signal strength, diffusion lengths measured from a wide range of samples were plotted as a function of V_{SPV} intensity (Fig. 3.69). The measured data exhibits relatively flat response; solid line is indicative of poor fit. The experiment suggests that extraction of diffusion length measurement is relatively invariant with strength of the surface photovoltage signal.

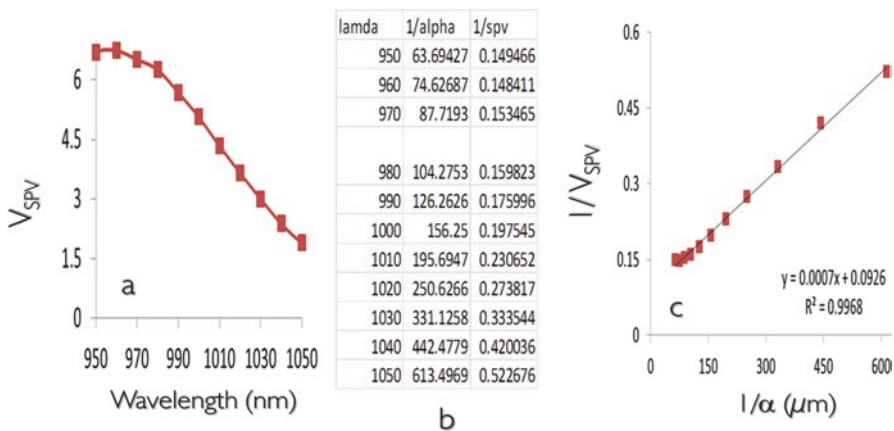


Fig. 3.66 Surface photovoltage approach to diffusion length measurements: (a) V_{SPV} data as a function of wavelength, (b) data for $1/\alpha$ and $1/V_{\text{SPV}}$, and plot of $1/\alpha$ versus $1/V_{\text{SPV}}$ including linear squares fit

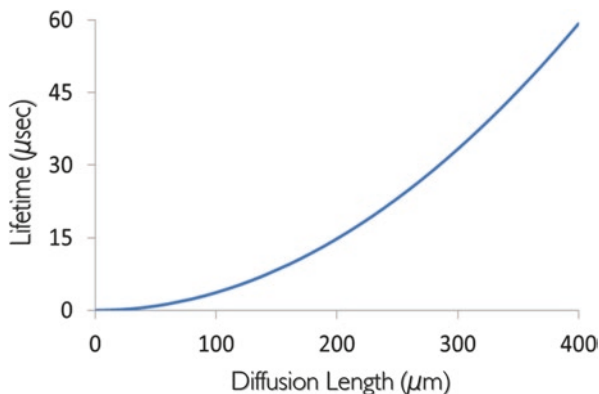
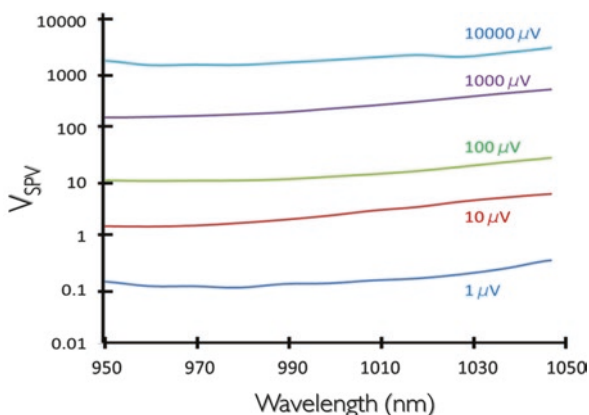


Fig. 3.67 Minority carrier lifetime plotted as a function of diffusion length

Fig. 3.68 Surface photovoltage measurement sensitivity over four orders of magnitude



SPV measurement resolution is illustrated in Fig. 3.70 for poor and high lifetime wafers with diffusion lengths up to 400- μm range; longer diffusion length measurement can also be measured. Influence of surface texture and emitter on diffusion lengths was also investigated. Figure 3.71 plots L_d measurements from p-type wafers after saw damage removal and subsequent alkaline texturing. Randomly textured surface exhibits a doubling of lifetime due to enhanced internal scattering and e-h pair generation. Similar measurements were carried out on POCl_3 -diffused wafers with phosphorous-doped oxide layer (Fig. 3.72). Similar behavior was observed with higher diffusion lengths. This method has also been used to evaluate surface passivation by plotting ratio of V_{SPV} signal before and after HF and boiling H_2O surface treatments (Fig. 3.73). Due to strong Si absorption at short wavelengths, V_{SPV} signal is expected to be a strong function of surface defects. Both HF and H_2O surface treatments are well-known for H-terminated passivation of Si

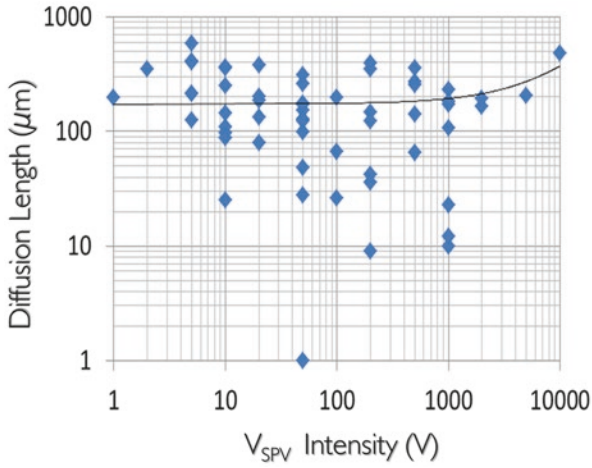


Fig. 3.69 Plot of diffusion lengths as a function of surface photovoltage intensity

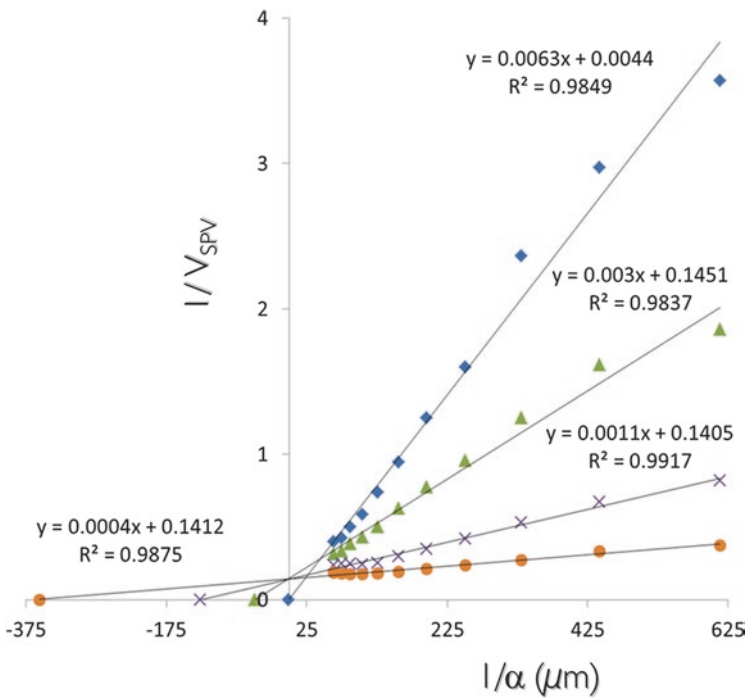


Fig. 3.70 Diffusion length measurements in ~1–400- μm range with acceptable R^2 values (~0.98–0.99)

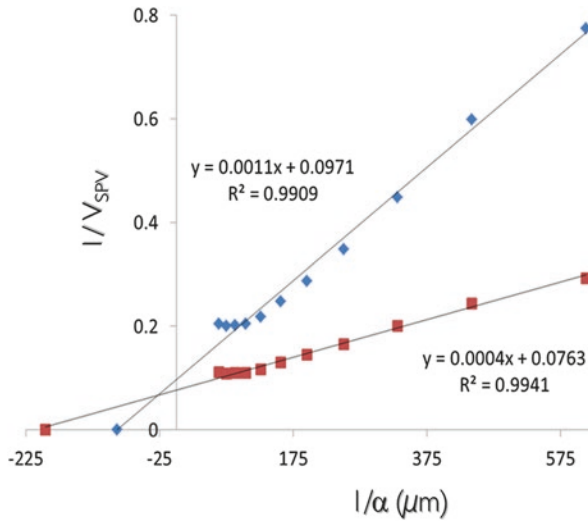


Fig. 3.71 Diffusion length measurements from p-type wafer planar ($L_d \sim 90 \mu\text{m}$) and textured ($L_d \sim 200 \mu\text{m}$) wafers

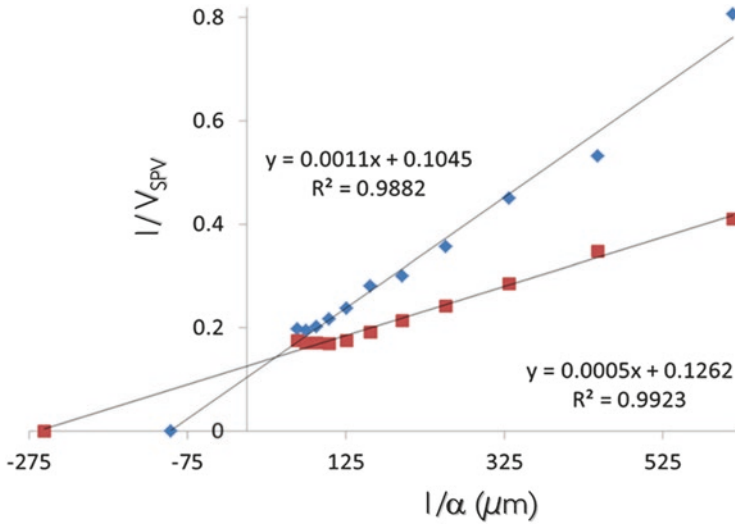


Fig. 3.72 Diffusion length measurements from p-type Si after POCl_3 diffusion and in situ phosphorous-doped SiO_2 on planar ($L_d \sim 100 \mu\text{m}$) and textured ($L_d \sim 260 \mu\text{m}$) wafers

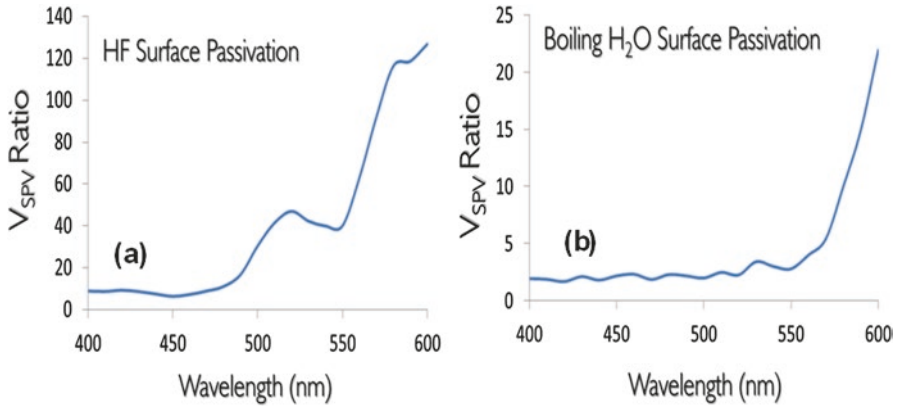


Fig. 3.73 Ratio of V_{SPV} signal after HF (a) and H_2O (b) surface treatments exhibiting formation of high-quality H-terminated surfaces resulting in reduction of surface recombination velocities

surfaces, which explains large signal enhancement due to reduced surface recombination velocity [62–64].

The surface photovoltage approach has been demonstrated to be highly effective in characterization of both low- and high-quality Si wafers with lifetimes in ~ 1 – 400 - μm range. Application of this method in UV-VIS range has been identified as a sensitive tool for surface passivation quality and recombination velocity. Finally, the measured L_d values were consistent with ~ 14 – 18% efficiency solar cells investigated in this study.

References

1. M.A. Green, M.J. Keevers, *Prog. Photovolt. Res. Appl.* **3**, 189 (1995)
2. See for instance, Concise Macleod Thin Film Software at www.thinfilcenter.com
3. P. Campbell, M.A. Green, *J. Appl. Phys.* **62**, 243 (1987)
4. P.A. Basore, 23rd IEEE PVSC, 147 (1993)
5. P. Sheng, A.N. Bloch, R.S. Stepleman, *Appl. Phys. Lett.* **43**, 579 (1983)
6. E. Yablonovitch, *J. O. S. A.* **72**, 899 (1982)
7. H.W. Deckmann, C.R. Wronski, H. Witzke, E. Yablonovitch, *Appl. Phys. Lett.* **42**, 968 (1983)
8. E. Hecht, A. Zajac, *Optics*, 2nd edn. (Addison-Wesley)
9. S.H. Zaidi, J.M. Gee, U.S. Patent 6, 858, 462 B2 (2005)
10. S.H. Zaidi, S.R.J. Brueck, 26th IEEE PVSC Proceedings, 171 (1997)
11. D.E. Aspnes, A.A. Studna, *Phys. Rev.* **B 27**, 985 (1983)
12. S.J. Wilson, M.C. Hutley, *Optica Acta* **29**, 993 (1982)
13. R.C. Enger, S.K. Case, *Appl. Opt.* **22**, 3220 (1983)
14. S.H. Zaidi, M. Yousaf, S.R.J. Brueck, *J. O. S. A.* **B 8**, 770 (1991)
15. K. Knop, *J.O.S.A.* **68**, 1206 (1978)

16. C. Heine, R.H. Morf, *Appl. Opt.* **34**, 2476 (1995)
17. S.H. Zaidi, A.-S. Chu, R.J. Brueck, *J. Appl. Phys.* **80**, 6997 (1996)
18. L. Rayleigh, *R. Soc. A* **79**, 399 (1907)
19. J.C. Botten, R.C. McPhedran, J.L. Adams, J.R. Andrewartha, *Optica Acta* **28**, 413 (1981)
20. M.G. Moharam, T.K. Gaylord, *J. O. S. A.* **71**, 811 (1981)
21. D.H. Raguin, G.M. Morris, *Appl. Opt.* **32**, 1154 (1993)
22. <http://www.gsolver.com/brochureV51.pdf>
23. S.H. Zaidi, S.R.J. Brueck, 26th IEEE PVSC, 171 (1997)
24. S. Zaidi, S.R.J. Brueck, Proceedings of SPIE 3740 Optical Engineering for Sensing and Nanotechnology, 340 (1999)
25. S.H. Zaidi, J.M. Gee, D.S. Ruby, S.R.J. Brueck, Proceedings of SPIE 3790 Engineered Nanostructured Films and Materials, 151 (1999)
26. S.H. Zaidi, J.M. Gee, D.S. Ruby, 28th IEEE PVSC, 395 (2000)
27. S.H. Zaidi, R. Marquardt, B. Minhas, J.W. Tringe, 29th IEEE PVSC, 1290 (2002)
28. S.H. Zaidi, C. Matzke, L. Koltunski, K. DeZetter, 30th IEEE PVSC, (2005)
29. S.G. Sandoval, M. Khizar, D. Modisette, J. Anderson, R. Manginell, N. Amin, K. Sopian, S.H. Zaidi, 35th IEEE PVSC (2010)
30. S.H. Zaidi, D.S. Ruby, J.M. Gee, Zaidi, *IEEE Trans. Elect. Dev.* **48**, 1200 (2001)
31. J.W. Goodman, *Introduction to Fourier Optics*, 2nd edn. (McGraw Hill Higher Education, 1996)
32. A.W. Azhari, A. Ali, K. Sopian, U. Hashim, S.H. Zaidi, Proceedings 40th IEEE PVSC (2014)
33. A.A. Istratov, H.H. Flink, T. Heiser, E.R. Weber, *Appl. Phys. Lett.* **71**, 2121 (1997)
34. M. Saritas, H.D. Mckell, *J. Appl. Phys.* **63**, 4561 (1988)
35. D.K. Schroder, *Semiconductor Material and Device Characterization* (Wiley, New York, 1990)
36. R.A. Sinton, A. Cuevas, *Appl. Phys. Lett.* **69**, 2510 (1996)
37. R.A. Sinton, A. Cuevas, M. Stuckings, Proceedings of IEEE PVSC-25, 457 (1997)
38. A. Cuevas, M. Stocks, D. Macdonald, R. Sinton, 2nd World PVSEC (1998)
39. A.M. Goodman, *J. App. Phys.* **32**, 2550 (1960)
40. D.K. Schroder, *IEEE Trans. Elec. Dev.* **44**, 160 (1997)
41. J.W. Orton, P. Blood, *The Electrical Characterization of Semiconductors: Measurement of Minority Carrier Properties (Techniques of Physics)* (Academic, 1990)
42. V.A. Focsa, A. Slaoui, J.C. Muller, I. Pelant, 3rd World PVSEC, 1040 (2003)
43. D.K. Schroder, *Meas. Sci. Technol.* **12**, R16 (2001)
44. L. Votoček, J. Toušek, Proceedings WDS-05, 595 (2005)
45. K. Kirilov, V. Donchev, T. Ivanov, K. Germanova, P. Vitanova, P. Ivanova, *J. Optoelectron. Adv. Mater.* **7**, 533 (2005)
46. https://www.helmholtz-berlin.de/forschung/oe/ee/si-pv/projekte/asicsi/afors-het/index_en.html
47. S. Ostapenko, I. Tarasov, J.P. Kalejs, C. Haessler, E.U. Reisner, *Semicond. Sci. Technol.* **15**, 840 (2000)
48. E. Daub, P. Klopp, S. Kugler, P. Würfel, *12th EPVSC* (Amsterdam, 1994)
49. P. Würfel, *Physics of Solar Cells* (Wiley-VCH, 2005)
50. P. Würfel, *J. Phys. C Solid State Phys.* **15**, 3967 (1982)
51. G. Smestad, H. Ries, *Solar Energy Mater. Solar Cells* **25**, 51 (1992)
52. T. Trupke, J. Zhao, A. Wang, R. Corkish, M.A. Green, *App. Phys. Lett.* **82**, 2996 (2003)
53. T. Trupke, R.A. Bardos, M.C. Schubert, W. Warta, *Appl. Phys. Lett.* **89**, 44107 (2006)
54. T. Trupke et al., 22nd European Photovoltaic Solar Energy Conference, 22 (2007)
55. M.A. Green, J. Zhao, A. Wang, P.J. Reece, M. Gal, *Nature* **412**, 805 (2001)
56. T. Fuyuki, H. Kondo, T. Yamazaki, Y. Takahashi, Y. Uraoka, *Appl. Phys. Lett.* **86**, 262108 (2005)
57. T. Fuyuki, H. Kondo, Y. Kazi, A. Ogana, Y. Takahashi, *J. Appl. Phys.* **101**, 023711 (2007)
58. A. Kitiyanan, A. Ogane, A. Tani, T. Hatayama, H. Yano, Y. Uraoka, T. Fukui, *J. Appl. Phys.* **106**, 043717 (2009)
59. Z.G. Ling, P.K. Ajmera, M. Anselment, L.F. Dimauro, *Appl. Phys. Lett.* **51**, 1445 (1987)
60. M. Bail, J. Kentsch, R. Brendel, M. Schulz, Proceedings of IEEE PVSC-28, 99 (2000)

61. S. Riepe, J. Isenberg, C. Ballif, S. Glunz, W. Warta, 17th Eu PVSEC, 1597 (2001)
62. S. Sepeai, C.S. Leong, K. Sopian, S.H. Zaidi, Proceedings 23rd IEEE PVSEC (2013)
63. D.B. Fenner, D.K. Biegelsen, R.D. Bringans, J. Appl. Phys. **66**, 419 (1989)
64. H. Angermann, P. Balamou, W. Lu, L. Korte, C. Leendertz, B. Stegemann, Solid State Phenomena **255**, 331 (2016)